aerospace

MDPI

Article

Autonomous Parafoil Flaring Control System for eVTOL Aircraft

Stephen Doran, Toufik Souanef * and James F. Whidborne

Centre for Aeronautics, Cranfield University, Bedford MK43 0AL, UK; doranstephen1@gmail.com (S.D.); j.f.whidborne@cranfield.ac.uk (J.F.W.)

* Correspondence: toufik.souanef@cranfield.ac.uk

Abstract: Reducing landing kinetic energy during emergency landings is critical for minimising occupant injury in eVTOL aircraft. This study presents the development of an autonomous parafoil control system for impact point targeting and flare control. A model predictive controller for a six-degree-of-freedom parafoil and eVTOL payload model was designed incorporating an inner-loop flare controller for descent speed-based flare height adjustments and an outer-loop nonlinear model predictive control (MPC) to minimize line-of-sight error. Two guidance methods were explored: a standard fixed impact point approach and an adaptive method that adjusts the target point dynamically to account for horizontal travel during flaring. The standard method outperformed the uncontrolled system in 79.64% of cases, while the adaptive method achieved success in 40.73% of scenarios, with both methods maintaining vertical landing velocities below 8 m/s in all tested cases. Controller performance degraded under higher wind speeds and large control derivative variations, with the adaptive method position error attributed to flare distance estimation inaccuracies.

Keywords: adaptive guidance; eVTOL; impact point targeting; landing position error; landing velocity; line of sight; model predictive control; nonlinear control; parafoil; six degrees of freedom

check for updates

Academic Editor: Mou Chen

Received: 18 December 2024
Revised: 4 February 2025
Accepted: 10 February 2025
Published: 14 February 2025

Citation: Doran, S.; Souanef, T.; Whidborne, J.F. Autonomous Parafoil Flaring Control System for eVTOL Aircraft. *Aerospace* **2025**, *12*, 145. https://doi.org/10.3390/aerospace12020145

Copyright: © 2025 by the authors. Licensee MDPI, Basel, Switzerland. This article is an open access article distributed under the terms and conditions of the Creative Commons Attribution (CC BY) license (https://creativecommons.org/licenses/by/4.0/).

1. Introduction

The anticipated increase in eVTOL aircraft operating in urban environments highlights the critical need for emergency autolanding capabilities. The Federal Aviation Authority advises that in the event of an emergency in which a powered aircraft cannot provide sufficient commanded thrust power, the aircraft must be capable of a controlled emergency landing: "by gliding or autorotation, or an equivalent means to mitigate the risk of loss of power or thrust" [1].

One "equivalent means" to execute the emergency landing is the use of a movable ballistic parafoil system. Thus, it is important to ensure that the landing velocity and kinetic energy of the system are minimized to reduce the likelihood of passenger injury and vehicle damage.

The study by [2] investigated crashworthiness in generic eVTOL aircraft configurations (high wing, low wing, mid-wing) with a maximum take-off mass of 1870 kg, focusing on the Dynamic Response Index (DRI)—a metric quantifying spinal injury risk during vertical impacts. Their finite element analysis revealed that vertical impact velocities exceeding 10 m/s surpassed the DRI threshold of 17.7 (associated with a 10% spinal injury probability [3]), while a maximum DRI of 17.6 at 8 m/s in the low-wing configuration suggested velocities below 8 m/s are necessary to reduce injury likelihood to <10%. This

underscores the criticality of minimizing vertical descent speeds for occupant safety, a challenge paralleled in parafoil systems where controlled landing maneuvers are employed to mitigate impact forces.

Parafoil systems achieve velocity reduction through flare maneuvers, which increase canopy angle of attack or camber to enhance lift and drag, thereby reducing horizontal and vertical speeds. Control strategies for trajectory optimization and terminal energy management are pivotal here. Prior research has emphasized trajectory tracking and energy minimization via PID, model predictive control (MPC), and neural networks. For instance, Ref. [4] established exponentially stable trajectory tracking using Lyapunov methods, later advanced by [5] with PID controllers optimized via particle swarm algorithms. Similarly, Refs. [6,7] integrated extended state observers to refine PID performance, while [8] implemented PID neural networks for adaptive control.

MPC approaches, as demonstrated by [9,10], outperformed PID in reducing landing errors under variable wind conditions by optimizing feed-forward and feedback gains. Nonlinear MPC further enhanced anti-windup robustness and tracking accuracy compared to PID, as shown by [11,12]. Trajectory optimization methods, such as those by [13,14], prioritized energy management and precise landing via convex programming, outperforming traditional guidance systems in minimizing position errors.

While prior studies have addressed parafoil landing challenges, they often treat trajectory tracking and flare execution as decoupled tasks, leading to suboptimal performance in real-world scenarios. This decoupling can result in conflicts between the desired IPI trajectory and the kinematic demands of the flare, such as insufficient horizontal or vertical travel distances, ultimately compromising landing safety. Additionally, many existing approaches lack adaptability to wind disturbances and payload variations due to their reliance on deterministic models or simplified control strategies. These limitations underscore the need for a unified control architecture that integrates guidance and flare execution while accommodating dynamic environmental conditions.

In this work, a control system that combines both nonlinear closed-loop MPC IPI targeting and open-loop bang-bang flaring control has been developed that allows for both accurate targeting and landing kinetic energy minimisation. Such a control system differs from previous developments by considering the condition-dependent horizontal and vertical distances travelled when performing the flare manoeuvre in the guidance strategy. Furthermore, the design allows for easy switching between control architecture types. Monte Carlo simulations are used to assess the performance of the control system.

The landing phase is divided into two parts: targeting the desired initial point of impact (IPI) using MPC line-of-sight (LOS) guidance, and executing the flare manoeuvre. In LOS guidance, the system's trajectory vector is directed towards the desired IPI.

The main contributions of the paper are:

- Dual-loop MPC design integrating inner flare control (descent speed-based height adjustments) and outer nonlinear MPC (LOS error minimization) for 6-DOF parafoil–eVTOL systems.
- Descent speed-adaptive flare controller for optimized energy dissipation.
- Comparison of fixed impact point vs. adaptive guidance methods for horizontal drift compensation during flaring.
- Real-time target point adaptation to account for flare-induced horizontal travel.

The paper is structured as follows: First, the nonlinear six-DOF model is presented in Section 2. Next, the design and implementation of the inner loop flare controller and outer loop MPC LOS controllers are described in Section 3. The results of the Monte Carlo simulations are then presented and discussed in Section 4. Finally, Section 5 concludes the paper.

2. Parafoil and eVTOL System Modelling

2.1. Background

This section presents the modelling and Simulink implementation of a six-DOF parafoil and eVTOL payload system. It is assumed that the parafoil has been fully inflated and hence is considered to be a fixed shape with the exception of the deformable brakes. The parafoil and eVTOL payload system are connected as a rigid body. The free body diagram of the system is shown in Figure 1.

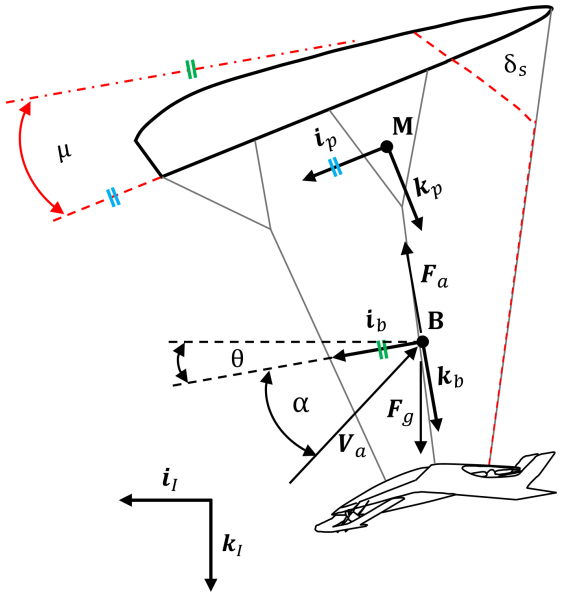

Figure 1. Six-DOF parafoil and eVTOL payload system free body diagram.

References to four axis systems are made in the proceeding derivations: the inertial Earth axes {I}, body axes {b}, wind axes {w}, and parafoil axes {p} systems.

- The x_I axis in the inertial Earth axes points east, the y_I axis points north, and the z_I axis points towards the centre of the Earth. The axis is centred at a specific point on the Earth's surface and is inertial.
- The body x_b axis points from tail to nose about the longitudinal symmetry plane of the system. The z_b axis is perpendicular to the x_b axis and is positive in the direction from canopy to payload (downwards). The z_b axis is perpendicular to the $x_b - z_b$ plane and is defined as positive using the right-hand rule. The axes system is centred at the parafoil and eVTOL payload system CG and is noninertial.
- The wind x_w axis is aligned with the incoming airflow and is defined as positive in the direction of the relative airflow. The y_w and z_w axes are defined in an equivalent manner to {b}. The parafoil x_p axis is aligned parallel to the lower surface of the parafoil (see Figure 1). The y_p and z_p axes are defined in an equivalent manner to {b}.

The rigging angle (μ) is defined as the angle between the body x_b axis and the parafoil x_p axis. Note that both μ and θ are negative in Figure 1.

2.2. Fundamental Equations

Following the derivation of [15], Newton's second law of motion in the nonrotating inertial coordinate frame I is given by:

$$\boldsymbol{F}^I = m\dot{\boldsymbol{V}} = m\begin{bmatrix}\dot{V}_x\\ \dot{V}_y\\ \dot{V}_z\end{bmatrix}, \tag{1}$$

where $\boldsymbol{F}^I$ is the force on the body in the inertial (Earth) reference frame and m is the mass. The x, y, and z accelerations in the inertial reference frames are denoted by $\dot{V}_x$, $\dot{V}_y$, and $\dot{V}_z$, respectively.

Now, consider the noninertial (rotating) body reference frame {b}. Accounting for the Coriolis force gives:

$$\boldsymbol{F} = m\dot{\boldsymbol{v}} + \boldsymbol{\omega} \times m\boldsymbol{v}, \tag{2}$$

where $\boldsymbol{v} = \begin{bmatrix}u\ v\ w\end{bmatrix}^T$ and $\boldsymbol{\omega} = \begin{bmatrix}p\ q\ r\end{bmatrix}^T$ are the vectors of linear and angular velocities in the {b} frame, respectively, and the operator $\times$ denotes the cross-product. Expanding gives

$$\begin{bmatrix}\dot{u}\\ \dot{v}\\ \dot{w}\end{bmatrix} = \frac{1}{m}\boldsymbol{F} - \boldsymbol{S}(\boldsymbol{\omega})\begin{bmatrix}u\\ v\\ w\end{bmatrix}, \quad \text{where} \quad \boldsymbol{S}(\boldsymbol{\omega}) = \begin{bmatrix}0 & -r & q\\ r & 0 & -p\\ -q & p & 0\end{bmatrix}. \tag{3}$$

Similarly, the rotational dynamics in the body {b} frame may be written as:

$$\boldsymbol{I}\begin{bmatrix}\dot{p}\\ \dot{q}\\ \dot{r}\end{bmatrix} = \boldsymbol{M} - \boldsymbol{S}(\boldsymbol{\omega})\boldsymbol{I}\begin{bmatrix}p\\ q\\ r\end{bmatrix}, \quad \text{where} \quad \mathbf{I} = \begin{bmatrix}I_{xx} & 0 & I_{xz}\\ 0 & I_{yy} & 0\\ I_{xz} & 0 & I_{zz}\end{bmatrix}. \tag{4}$$

Here, $\boldsymbol{I}$ is the inertia matrix and $\boldsymbol{M}$ is the moment vector in {b}. Symmetry is assumed about the $x_b - z_b$ plane.

Combining Equations (3) and (4) gives:

$$\left[\begin{array}{c|c}(m+m_e)\boldsymbol{I}_{3\times3} & \boldsymbol{0}_{3\times3}\\ \hline \boldsymbol{0}_{3\times3} & \boldsymbol{I}_{3\times3}\end{array}\right]\begin{bmatrix}\dot{u}\\ \dot{v}\\ \dot{w}\\ \hline \dot{p}\\ \dot{q}\\ \dot{r}\end{bmatrix} = \begin{bmatrix}\boldsymbol{F} - (m+m_e)\boldsymbol{S}(\boldsymbol{\omega})\begin{bmatrix}u\\ v\\ w\end{bmatrix}\\ \hline \boldsymbol{M} - \boldsymbol{S}(\boldsymbol{\omega})\boldsymbol{I}\begin{bmatrix}p\\ q\\ r\end{bmatrix}\end{bmatrix}, \tag{5}$$

where m_e denotes the mass entrapped in the canopy and $\boldsymbol{0}_{3\times3}$ and $\boldsymbol{I}_{3\times3}$ represent 3×3 zero and identity matrices, respectively.

2.3. Forces and Moments

The forces acting in {b} consist of gravitational forces, aerodynamic forces, and forces due to apparent mass. For simplicity, the aerodynamic forces are modelled as a combination of the payload and canopy contributions.

The gravitational forces are given by:

$$\boldsymbol{F}_g = mg\begin{bmatrix}-\sin\theta\\ \cos\theta\sin\phi\\ \cos\theta\cos\phi\end{bmatrix}, \tag{6}$$

where θ, ϕ, and ψ are the Euler pitch, roll, and yaw angles in {b}, respectively. The matrix transformation required to obtain these is discussed later in this section.

The aerodynamic forces in {b} are modelled using aero derivatives as follows:

$$\boldsymbol{F}_a = QS_w^b \boldsymbol{R} \begin{bmatrix} C_{D_0} + C_{D_{\alpha^2}}\alpha^2 + C_{D_{\delta_s}}\delta_s + C_{D_{\delta_\mu}}\delta_\mu \\ C_{Y_\beta}\beta \\ C_{L_0} + C_{L_\alpha}\alpha + C_{L_{\delta_s}}\delta_s + C_{L_{\delta_\mu}}\delta_\mu \end{bmatrix}, \tag{7}$$

where δ_a and δ_s refer to the asymmetric and symmetric brake deflections, respectively normalised between $[0, 1]$. A unit brake deflection indicates the maximum permissible brake deflection. δ_μ refers to the change in rigging angle from its trim value. Q is the dynamic pressure and is given by:

$$\frac{\rho |\boldsymbol{V}_a|^2}{2}, \tag{8}$$

and S is the canopy area. $\boldsymbol{V}_a$ is the airspeed vector and is given by $\boldsymbol{V}_a = \boldsymbol{V} - \boldsymbol{W}$, where $\boldsymbol{V}$ is the groundspeed vector in {b}, and $\boldsymbol{W}$ is the windspeed vector in {b}. ${}^b_w\boldsymbol{R}$ is the rotation matrix from wind axes (where the aerodynamic derivatives are typically defined) to the body axes.

The angle of attack (α) and sideslip angle (β) are defined using the airspeed vector as follows:

$$\alpha = \tan^{-1}\left(\frac{v_z}{v_x}\right), \quad \beta = \tan^{-1}\left(\frac{v_y}{\sqrt{v_x^2 + v_z^2}}\right).$$

The direction cosine matrix (DCM) transformation from the Earth axes to the body axes (${}^b_n\boldsymbol{R}$) is given by:

$$\begin{aligned} {}^b_n\boldsymbol{R} &= \boldsymbol{R}_\psi \boldsymbol{R}_\theta \boldsymbol{R}_\phi = \\ &\begin{bmatrix} \cos\theta\cos\psi & \cos\theta\sin\psi & -\sin\theta \\ -\cos\phi\sin\psi + \sin\phi\sin\theta\cos\psi & \cos\phi\cos\psi + \sin\phi\sin\theta\sin\psi & \sin\phi\cos\theta \\ \sin\phi\sin\psi + \cos\phi\sin\theta\cos\psi & -\sin\phi\cos\psi + \cos\phi\sin\theta\sin\psi & \cos\phi\cos\theta \end{bmatrix}. \end{aligned} \tag{9}$$

Similarly, ${}^b_w\boldsymbol{R}$ is given by:

$${}^b_w\boldsymbol{R} = \boldsymbol{R}_\alpha \boldsymbol{R}_\beta = \begin{bmatrix} \cos\alpha\cos\beta & \cos\alpha\sin\beta & -\sin\alpha \\ -\sin\beta & \cos\beta & 0 \\ \sin\alpha\cos\beta & \sin\alpha\sin\beta & \cos\alpha \end{bmatrix}.$$

The aerodynamic moments in {b} are modelled as

$$\boldsymbol{M}_a = \frac{\rho |\boldsymbol{V}_a|^2 S}{2} \begin{bmatrix} b\left(C_{l_\beta}\beta + \frac{b}{2V_a}C_{l_p}p + \frac{b}{2V_a}C_{l_r}r + C_{l_{\delta_a}}\delta_a\right) \\ c\left(C_{m_0} + C_{m_\alpha}\alpha + \frac{c}{2V_a}C_{m_q}q\right) \\ b\left(C_{n_\beta}\beta + \frac{b}{2V_a}C_{n_p}p + \frac{b}{2V_a}C_{n_r}r + C_{n_{\delta_a}}\delta_a\right) \end{bmatrix}. \tag{10}$$

where b is the canopy wingspan and c is the mean canopy chord length. It can be seen that an asymmetric brake deflection is used for roll and yaw rate control and a symmetric brake deflection is used for x and z axis velocity control in {b}.

The derivation of the apparent forces and moments is not presented in this paper but is covered extensively in [15].

In conclusion, the forces arising from the apparent mass and moment arising from the apparent inertia in {b} are given as:

$$\begin{aligned}\boldsymbol{F}_{a.m.} = &-{}^{p}_{b}\boldsymbol{R}^{T}\left[\boldsymbol{I}_{a.m.}{}^{p}_{b}\boldsymbol{R}\left(\begin{bmatrix}\dot{u}\\ \dot{v}\\ \dot{w}\end{bmatrix} - \boldsymbol{S}(\boldsymbol{r}_{BM})\begin{bmatrix}\dot{p}\\ \dot{q}\\ \dot{r}\end{bmatrix}\right)\right.\\ &\left.+{}^{p}_{b}\boldsymbol{R}\boldsymbol{S}(\boldsymbol{\omega}){}^{p}_{b}\boldsymbol{R}^{T}\boldsymbol{I}_{a.m.}{}^{p}_{b}\boldsymbol{R}\left(\begin{bmatrix}u\\ v\\ w\end{bmatrix} - \boldsymbol{S}(\boldsymbol{r}_{BM})\begin{bmatrix}p\\ q\\ r\end{bmatrix} - {}^{b}_{n}\boldsymbol{R}\boldsymbol{W}\right)\right]\\ \boldsymbol{M}_{a.i.} = &-{}^{p}_{b}\boldsymbol{R}^{T}\left(\boldsymbol{I}_{a.i.}{}^{p}_{b}\boldsymbol{R}\begin{bmatrix}\dot{p}\\ \dot{q}\\ \dot{r}\end{bmatrix} + {}^{p}_{b}\boldsymbol{R}\boldsymbol{S}(\boldsymbol{\omega}){}^{p}_{b}\boldsymbol{R}^{T}\boldsymbol{I}_{a.i.}{}^{p}_{b}\boldsymbol{R}\begin{bmatrix}p\\ q\\ r\end{bmatrix}\right) + \boldsymbol{S}(\boldsymbol{r}_{BM})\boldsymbol{F}_{a.m.},\end{aligned} \tag{11}$$

where $\boldsymbol{r}_{BM}$ is the displacement vector from the body axes centre to the parafoil axes centre. The skew matrix $\boldsymbol{S}(\boldsymbol{r}_{BM})$ is defined in the same way as (4). $\boldsymbol{M}_{a.m.}$ and $\boldsymbol{I}_{a.i.}$ are the apparent mass and inertia identity matrices, respectively, and are given by:

$$\boldsymbol{I}_{a.m.} = \begin{bmatrix}A & 0 & 0\\ 0 & B & 0\\ 0 & 0 & C\end{bmatrix}, \quad \boldsymbol{I}_{a.i.} = \begin{bmatrix}I_A & 0 & 0\\ 0 & I_B & 0\\ 0 & 0 & I_C\end{bmatrix}. \tag{12}$$

From [16], the apparent masses are given by:

$$A = 0.666 \cdot \rho \cdot \left(1 + \frac{8}{3} \cdot a^{*2}\right) \cdot t^2 \cdot b, \tag{13}$$

$$B = 0.267 \cdot \rho \cdot \left(1 + 2 \cdot \frac{a^{*2}}{t^{*2}} \cdot AR \cdot \left(1 - t^{*2}\right)\right) \cdot t^2 \cdot c, \tag{14}$$

$$C = 0.785 \cdot \rho \cdot \sqrt{1 + 2 \cdot a^{*2} \cdot (1 - t^{*2})} \cdot \frac{AR}{1 + AR} \cdot c^2 \cdot b, \tag{15}$$

and the apparent inertias by

$$I_A = 0.055 \cdot \rho \cdot \frac{AR}{1 + AR} \cdot c^2 \cdot b^3, \tag{16}$$

$$I_B = 0.0308 \cdot \rho \cdot \frac{AR}{1 + AR} \cdot \left[1 + \frac{\pi}{6} \cdot (1 + AR) \cdot AR \cdot a^{*2} \cdot t^{*2}\right] \cdot c^4 \cdot b, \tag{17}$$

$$I_C = 0.0555 \cdot \rho \cdot \left(1 + 8 \cdot a^{*2}\right) \cdot t^2 \cdot b^3, \tag{18}$$

where:

$$AR = \frac{b}{c}, \qquad t^* = \frac{t}{c}, \qquad a^* = \frac{a}{b}, \tag{19}$$

and where b is the inflated parafoil canopy span, c is the inflated parafoil canopy chord thickness, and a is the height from the centre of the inflated parafoil horizontal datum (lowest point of the inflated parafoil) to the point on the top surface of the centre of the inflated canopy [17].

2.4. Kinematic and Navigation Equations

The rotational kinematic angular accelerations are obtained as follows:

$$\begin{bmatrix}\dot{\phi}\\ \dot{\theta}\\ \dot{\psi}\end{bmatrix} = \begin{bmatrix}1 & \sin\phi\tan\theta & \cos\phi\tan\theta\\ 0 & \cos\phi & -\sin\phi\\ 0 & \sin\phi\sec\theta & \cos\phi\sec\theta\end{bmatrix}\begin{bmatrix}p\\ q\\ r\end{bmatrix}, \tag{20}$$

where the matrix to the left of $[p\ q\ r]^T$ is the transformation matrix from body axes rates to Euler rates. Integrating the above equation returns the values of ϕ, θ, and ψ (Euler angles) and thus the gravitational forces in (6) may be calculated.

The navigation velocities in {I} are calculated as follows:

$$\begin{bmatrix} \dot{P}_N \\ \dot{P}_E \\ \dot{P}_D \end{bmatrix} = \begin{bmatrix} V_N \\ V_E \\ V_D \end{bmatrix} = {}^{b}_{n}\boldsymbol{R}^T \begin{bmatrix} u \\ v \\ w \end{bmatrix}, \tag{21}$$

where the transpose of ${}^{b}_{n}\boldsymbol{R}$ is used as the transformation is from body to Earth axes. Equation (21) returns the groundspeed values in the Earth axes. Note that these values are not required for the creation of the six-DOF model but are used in the GNC algorithms.

2.5. Complete Equations of Motion

Substituting the forces and moments into (5), rearranging, and presenting in a compact form gives:

$$\dot{\boldsymbol{V}}^* = (\boldsymbol{A}_U + \boldsymbol{A}_r\boldsymbol{A}_L)^{-1}\left\{ \begin{bmatrix} \boldsymbol{F}_a + \boldsymbol{F}_g \\ \boldsymbol{M}_a \end{bmatrix} - \left[\boldsymbol{A}_\omega\boldsymbol{A}_U + \boldsymbol{A}_r\boldsymbol{A}_\omega\boldsymbol{A}_L - \boldsymbol{A}_r\boldsymbol{S}(\boldsymbol{\omega})\boldsymbol{I}'_{a.m.}\,{}^{b}_{n}\boldsymbol{R}\boldsymbol{W}\right]\boldsymbol{V}^* \right\}, \tag{22}$$

where $\boldsymbol{V}^* = \left[u\ v\ w\ p\ q\ r\right]^T$, and the matrices $\boldsymbol{A}_U$, $\boldsymbol{A}_L$, $\boldsymbol{A}_r$, and $\boldsymbol{A}_\omega$ are given by

$$\begin{gathered} \boldsymbol{A}_U = \begin{bmatrix} (m+m_e)\boldsymbol{I}_{3\times3} + \boldsymbol{I}'_{a.m.} & \boldsymbol{I}'_{a.m.}\boldsymbol{S}(\boldsymbol{r}_{BM}) \\ \boldsymbol{0_{3\times3}} & \boldsymbol{I} + \boldsymbol{I}'_{\text{a.i.}} \end{bmatrix}, \quad \boldsymbol{A}_r = \begin{bmatrix} \boldsymbol{I}_{3\times3} & \boldsymbol{0}_{3\times3} \\ \boldsymbol{0}_{3\times3} & \boldsymbol{S}(\boldsymbol{r}_{BM}) \end{bmatrix}, \\ \boldsymbol{A}_L = \begin{bmatrix} \boldsymbol{0}_{3\times3} & \boldsymbol{0}_{3\times3} \\ \boldsymbol{I}'_{a.m} & \boldsymbol{I}'_{a.m.}\boldsymbol{S}(\boldsymbol{r}_{BM}) \end{bmatrix}, \quad \boldsymbol{A}_\omega = \begin{bmatrix} \boldsymbol{S}(\boldsymbol{\omega}) & \boldsymbol{0}_{3\times3} \\ \boldsymbol{0}_{3\times3} & \boldsymbol{S}(\boldsymbol{\omega}). \end{bmatrix}. \end{gathered} \tag{23}$$

Note that standard notation has been used for tensors of second rank, i.e., $\boldsymbol{I}'_{\xi} = {}^{p}_{b}\boldsymbol{R}^T\boldsymbol{I}_{\xi_b}\,{}^{p}_{b}\boldsymbol{R}$. Equations (22) and (23) present the complete six-DOF equations of motion.

2.6. Mass, Inertial, and Dimensional Properties

The Aston Martin Volante Vision concept eVTOL aircraft shown in Figure 2 is used as the payload in this paper; details are available in [18]. The aircraft uses rotor tilt, rotor power, and elevator deflection for longitudinal control and rotor tilt, rotor power, aileron deflection, and rudder deflection for lateral/directional control. It is important to note that only the mass and inertial properties of this aircraft are used in the six-DOF model. The aerodynamic and control derivatives for a parafoil and payload system have been obtained from the literature as is later explained.

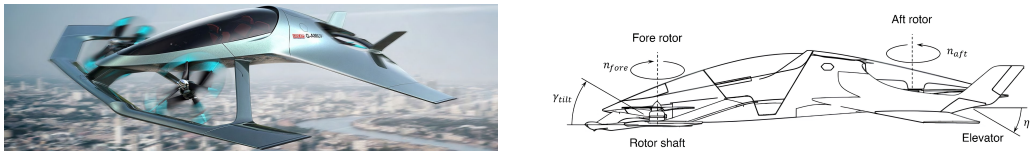

(**a**) Three-dimensional render (**b**) Longitudinal controls

Figure 2. The Aston Martin Volante Vision concept eVTOL aircraft.

The mass and inertial properties are presented in Table 1 below. All off-diagonal inertias have been set to zero as their magnitude is negligible in comparison to the I_{xx}, I_{yy}, and I_{zz} components. m_b refers to the body (payload) mass.

Table 1. eVTOL mass and inertial properties.

m_b (kg)	I_{xx} (kgm^2)	I_{yy} (kgm^2)	I_{zz} (kgm^2)
2100	1.0608×10^4	3.5554×10^4	4.5921×10^4

The inertia of the canopy structure is ignored; however, the significant mass and inertia of air displaced by the canopy are included in the apparent mass and inertia matrices as was described in Section 2.3.

The canopy dimensions and mass were linearly scaled from [19] based on a payload mass of 1255 kg, approximately 0.6 times the mass of the Volante Vision eVTOL concept. In comparison, the NASA X-38 program parafoil was tested with a minimum payload mass of 6800 kg, 3.25 times the eVTOL mass. As such, a mass scaling factor was defined as $SF_m = m_b/1255$, resulting in the canopy properties defined in Table 2. m_p refers to the mass of the parafoil canopy.

Table 2. Parafoil canopy mass and dimensions.

m_p (m)	b (m)	c (m)	t (m)	S (m^2)	a (m)	AR (-)
500	23.928	9.705	1.456	232.221	3.614	2.466

The displacement vector $\boldsymbol{r}_{bm}$ was determined by scaling the NASA X-38 program dimensions as visible in Appendix A.2, Figure A4. Note that it has been assumed that the CG of the system lies at the approximate centroid of the crew return vehicle, which is untrue as the apparent mass of air displaced by the canopy is significant. To encounter for error in the determination of the CG, a 5% standard deviation variation is placed on the distances in the later Monte Carlo simulations. The displacement vector is given by

$$\begin{aligned} \boldsymbol{r}_{BM} &= [1.41/SF_m,\ 0,\ -33.02/SF_m]\ \text{m}, \\ &= [0.5777,\ 0,\ -13.5297]\ \text{m}. \end{aligned} \tag{24}$$

where the x, y, and z distances in the first line refer to the distances obtained from the X-38 program. These distances were then linearly scaled using the mass scaling factor.

2.7. Aerodynamic and Control Derivatives

Following the same method of determining the dimensional properties of the canopy, the aerodynamic and control derivatives were obtained from the similarly sized system of [19]. An analysis of these aerodynamic and control derivatives shows that they were obtained from [15] for the Snowflake PADS vehicle, which has a system mass of 2.4 kg. Thus, scaling errors are likely when using these values on a significantly larger system. Table 3 presents the aerodynamic and control derivative values.

Table 3. Parafoil with eVTOL payload aerodynamic and control derivatives.

Aerodynamic Derivatives				**Control Derivatives**			
C_{D_0}	0.25	$C_{D_{\alpha^2}}$	0.12/rad^2	$C_{D_{\delta_s}}$	0.21	$C_{L_{\delta_s}}$	0.40
C_{Y_β}	−0.23/rad	C_{L_0}	0.091	$C_{D_{\delta_\mu}}$	2.0/rad	$C_{L_{\delta_\mu}}$	3.95/rad
C_{L_α}	0.90/rad	C_{l_β}	−0.036/rad	$C_{l_{\delta_a}}$	−0.0035	$C_{n_{\delta_a}}$	0.0015
C_{l_p}	−0.84/(rad/s)	C_{l_r}	−0.08/(rad/s)				
C_{m_0}	0.35	C_{m_α}	−0.7/rad				
C_{m_q}	−1.49/(rad/s)	C_{n_β}	−0.0015/rad				
C_{n_p}	0.082/(rad/s)	C_{n_r}	−0.27/(rad/s)				

The lift effects of the small aspect ratio wings in the Aston Martin Volante Vision concept have been ignored and the rotors are assumed to be feathered into the wind.

As the Snowflake PADS has controls of asymmetric and symmetric brake deflection only, the μ derivatives in Table 3 were obtained from the X-38 program [20].

2.8. Simulink Implementation

As longitudinal motion only is of interest, the values of $\dot{v}$, $\dot{p}$, and $\dot{r}$ in the equations of motion block were set to zero and the asymmetric brake deflection control was not modelled. Therefore, it is assumed that a wing leveller control system exists and the body x axis is directly aligned with the headwind resulting in no sideslip. Figure 3 presents the full six-DOF model of the controlled system. The controller acts on the outside of this model and will be described in the proceeding sections.

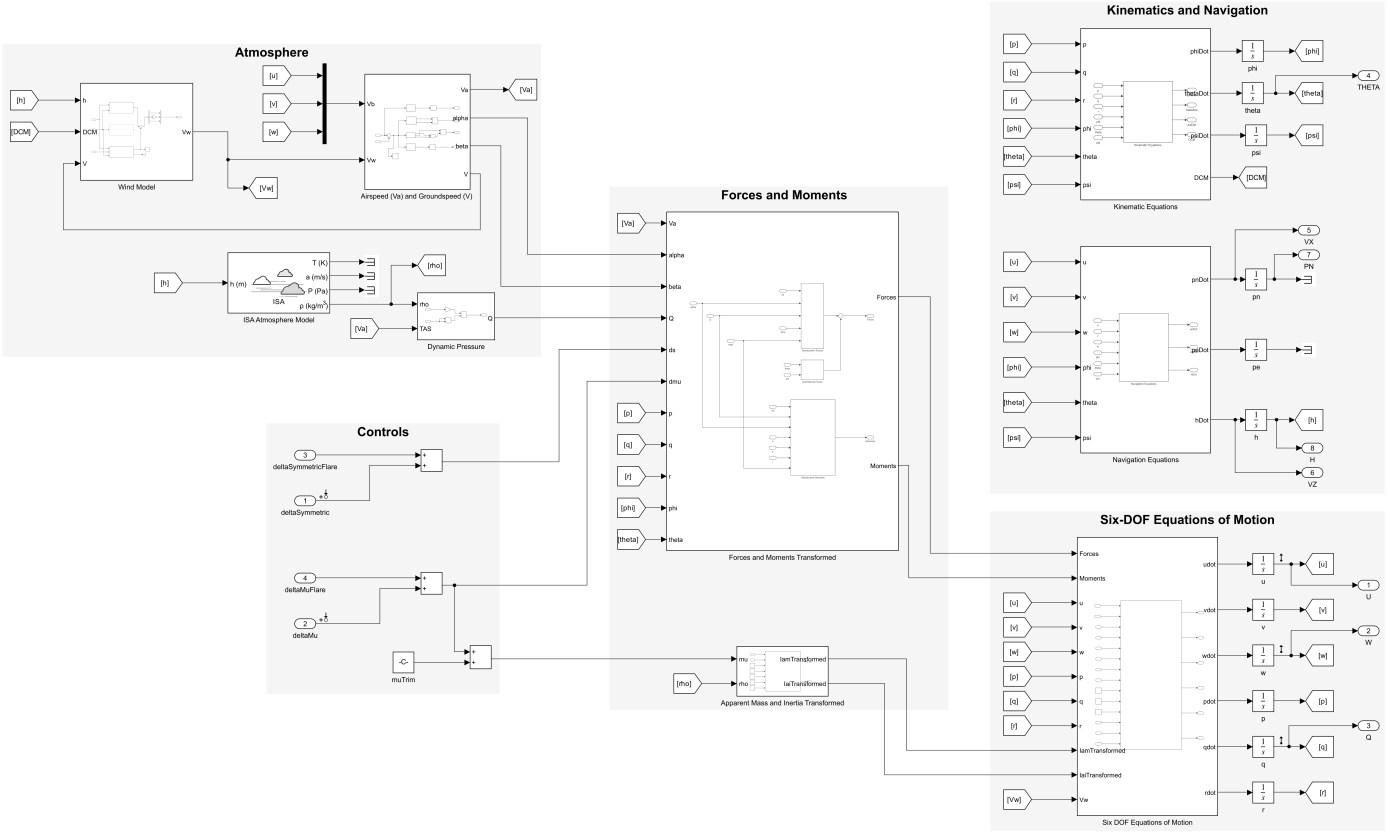

Figure 3. Simulink implementation of six-DOF model.

The model was automatically trimmed before each run using the MATLAB `findop` function and setting the states of u, w, q, θ, and P_N to an unknown steady-state value and h to an unknown non-steady-state value. Linearisation occurred about this trim point using the MATLAB `linearize` function with inputs of δ_s and δ_μ and outputs of u, w, q, and θ. Any additional variables that arose from the linearisation process were automatically removed by truncating the resulting state space matrix.

Ultimately the linearisation process returns the linear state space form of the system:

$$\dot{\boldsymbol{x}} = \boldsymbol{A}\boldsymbol{x} + \boldsymbol{B}\boldsymbol{u},$$
$$\boldsymbol{y} = \boldsymbol{C}\boldsymbol{x} + \boldsymbol{D}\boldsymbol{u}.$$

where $\boldsymbol{x}$ is the vector of change in state values from the trim values, $\boldsymbol{u}$ is the vector of change in control inputs from the trim control inputs, and $\boldsymbol{y}$ is the vector of output values u, w, q and θ for each entry in $\boldsymbol{x}$ and $\boldsymbol{u}$.

In emergency landing scenarios, the wind shear caused by the boundary layer on the surface of the Earth is significant. The Simulink "Wind Shear Model" block was implemented in the model to account for this. From [21], the mathematical wind shear model used in this block is [22]

$$u_w = W_{20} \frac{\ln(h/z_0)}{\ln(20/z_0)} \tag{25}$$

where u_w is the resultant mean wind speed, W_{20} is the wind speed at 20 ft (6 m), h is the height, and z_0 is a constant equal to 0.15 ft/s in Category C flight phases and 2 ft/s in all other flight phases. Note that the metric version of this block in Simulink was implemented and thus the inputs and outputs are SI units.

Figure 4 shows the wind shear for horizontal wind speeds at 6 m of $\{1, 2, 3, 4, 5\}$ m/s and a height range of $[0, 500]$ m.

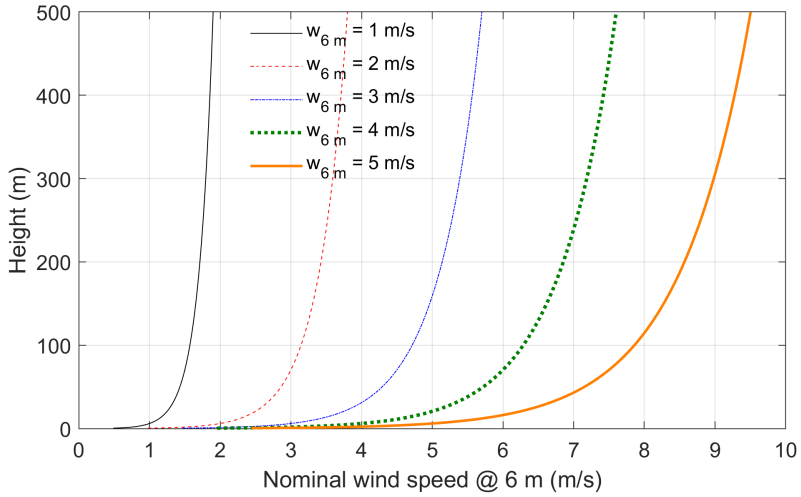

Figure 4. Wind shear visualisation for heights of 0–500 m and horizontal wind speeds at 6 m of 1–5 m/s.

It can be seen that the wind speed gradient is significant at large $w_{6\text{ m}}$. A parafoil and payload system that is in trim at a nominal height will quickly be out of trim as the wind speed changes rapidly. At small $w_{6\text{ m}}$, the gradient is minimal and the out-of-trim effects may not be observed until close to the ground where the gradient changes rapidly. A wind speed of 5 m/s (9.72 kt) at 6 m corresponds to a wind speed of 9.5 m/s (18.50 kt) at 500 m, representing a 90% increase.

In addition to wind shear, turbulence in the north and down {I} directions was incorporated using the continuous Dryden wind turbulence model [22] with a noise sample time of 0.1 s. The default scale length of 533.4 m was used with a small (10^{-2}) probability of exceeding high-altitude intensity. Turbulence is generated by passing band-limited white noise through forming filters. The rotational velocity of the wind was ignored and turbulence in the body y axis was set to zero as the parafoil and eVTOL payload system is assumed to be flying directly north into a headwind. Note that both the wind shear and Dryden wind turbulence are defined in the Earth axes frame {I} and are transformed to the body axes frame {b} using the direction cosine matrix as defined in (9).

2.9. Model Testing

Linearisation of the model at heights of $[100, 500]$ m and nominal wind speeds at 6 m of $[0, 5]$ m/s showed a short period pitching oscillation with a damping ratio of approximately 0.68 and a period of approximately 1.28 s. The phugoid mode was shown to be fully

damped with a period of approximately 269 s, which may be explained by the very high damping of the system (phugoid damping is inversely proportional to the lift-to-drag ratio). The resultant pole corresponded to a fully damped high-frequency mode (HFM) with a negligible period of 8×10^{-4} s. The frequency and damping of the modes were found to remain approximately constant with variations in height and wind speed over the tested range.

The step responses of the system to a one-unit d_s step and 5° δ_μ step for the conditions described above are presented in Figures 5–7.

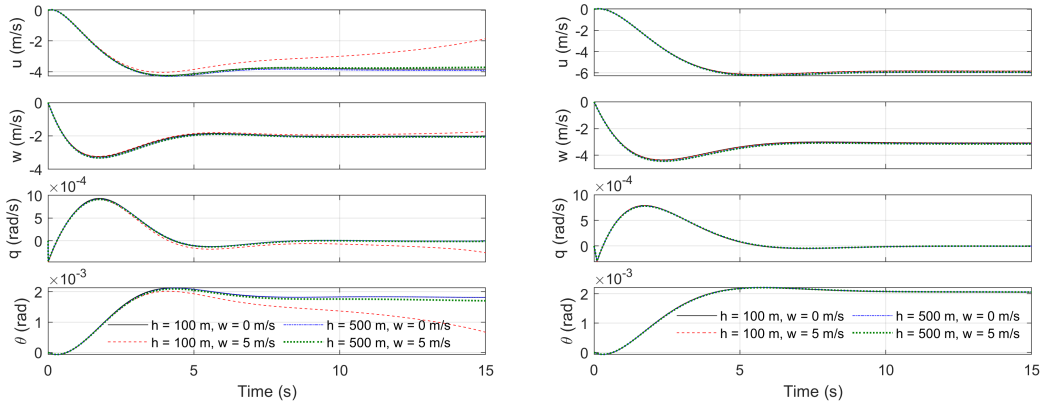

(**a**) One-unit d_s step input to nonlinear model (**b**) One-unit d_s step input to linear model

Figure 5. Nonlinear and linear models response to 1 unit δ_s step control input at various heights and nominal wind conditions at 6 m.

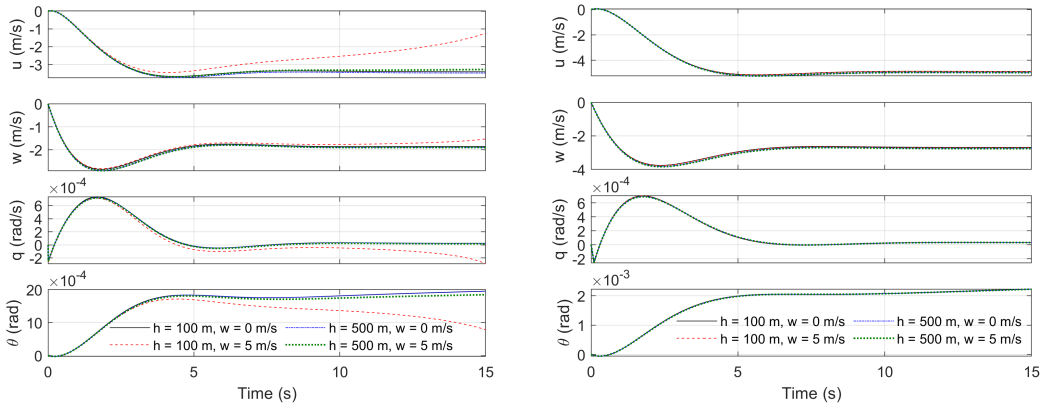

(**a**) Five-degree step input to nonlinear model (**b**) Five-degree step input to linear model

Figure 6. Nonlinear and linear models response to 5° d_μ step control input at various heights and nominal wind conditions at 6 m.

The negligible effect of the HFM is visible in the q responses of both the nonlinear and linear systems. Figures 5–7 show that little difference in the step responses for each condition is present except for at a height of 100 m and nominal wind speed at 6 m of 5 m/s. Referring to Figure 4, it can be seen that the wind shear effects within the dynamics time frame of 15 s are significant for this condition. The effects of this concerning the flare manoeuvre are notable as it occurs close to the ground. The difference in u and w values at the peak time for the different conditions is minor; however, the difference in u and w values at the settling time is considerable for the height of 100 m and nominal wind speed at 6 m of 5 m/s response. The controls have little effect on q and the resultant θ. This can be explained by the assumption that the centre of lift lies above the body axes centre and thus the moment control derivatives were not modelled.

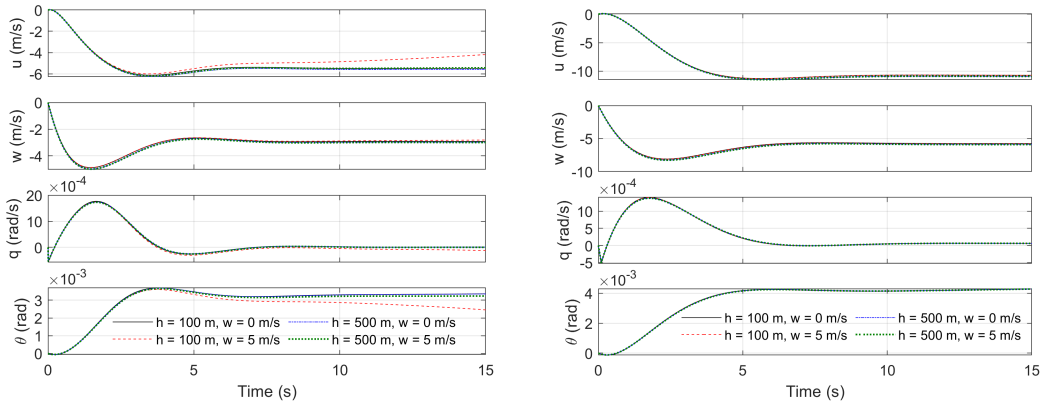

Figure 7. Nonlinear and linear models response to 5° d_μ step control input at various heights and nominal wind conditions at 6 m. (**a**) Combined 1-unit d_s and 5° d_μ step input to nonlinear model. (**b**) Combined 1-unit d_s and 5° d_μ step input to linear model.

Figures 5–7 show that the linear model adequately captures the shape of the responses. The step responses for each condition are approximately identical as the linear model does not account for wind shear. The u and w peak responses are overestimated by 24.1% and 33.7%, respectively for the δ_s step input. For the δ_{mu} step input, overestimates of 40.2% and 32.1% occur. The combined control input overestimates the u and w responses by 85.0% and 65.7%, respectively. As expected, the error was greatest for the combined response as the superposition principle was used in the linear system response, i.e., the combined response was taken to be the addition of the δ_s and δ_μ responses.

It is important to note that although the linear system overestimates the u and w peak responses, the error in the w/u ratio is considerably less as shown in Table 4.

Table 4. u and w responses of nonlinear and linear systems to step control inputs.

System	Control Input	u_{peak} (m/s)	w_{peak} (m/s)	$\frac{w}{u}$ Ratio	$\frac{w}{u}$ Ratio % Difference
Nonlinear	δ_s (1 unit step)	4.77	3.32	0.696	-
	δ_μ (5° step)	3.73	2.9	0.777	-
	Combined	6.21	4.99	0.804	-
Linear	δ_s (1 unit step)	6.26	4.44	0.709	1.903
	δ_μ (5° step)	5.23	3.83	0.732	5.809
	Combined	11.49	8.27	0.720	10.427

A maximum error of 10.427% occurs in the w/u ratio for the system with a combined control input. Therefore, the following conclusions can be made:

- The linear system may be used in the MPC control if the cost function includes the ratio of w/u. Similarly, the ratio v_z/v_x could be included in the cost function. The error in these ratios is relatively small when comparing the linear system to the nonlinear system.
- Therefore, a line of sight cost function involving the angle to the desired point of impact can be utilised as it uses the ratio of w/u.
- Alternatively, the nonlinear system may be used for MPC control to increase the accuracy of the guidance but with an associated increase in computational cost.

3. Controller Design and Implementation

3.1. Background

In the event of an emergency landing scenario, sufficient height may not be available to target the desired IPI. In such situations, it is useful to have an independent flare control system that deploys based on the current state and control values of the system. This section presents the design of a controller for desired IPI targeting and terminal velocity/kinetic energy minimisation. The design philosophy and implementation of the inner loop flare controller are first described, followed by the outer loop MPC IPI targeting control system. The final section describes the Monte Carlo simulation setup used to test the performance of the control system.

3.2. Inner Loop Flare Controller

3.2.1. Theory

Consider the step response of the linear system at a height of 100 m and zero wind as shown in Figure 8.

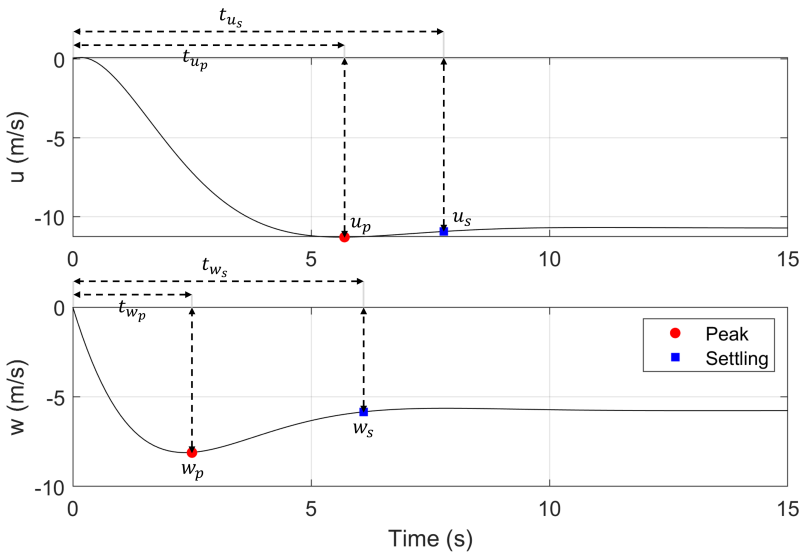

Figure 8. Combined 1-unit d_s and 5° d_μ step response metrics and a height of 100 m and nominal wind speed at 6 m of 0 m/s.

As the trim θ is approximately 0 rad, the change in θ resulting from a step input is negligible (see Figures 5–7), and the motion is confined to the longitudinal plane only, the following relation holds:

$$v_x \approx u, \qquad v_z \approx w. \tag{26}$$

Using the superposition property of a linear-time-invariant (LTI) system, the peak time and settling times shown in Figure 8 are independent of the step magnitude. Two flare settings can be defined as follows:

- Vertical velocity reduction flare setting: results in the minimum vertical velocity and is based on the w peak response only (w_p and t_{w_p}).
- Kinetic energy reduction flare setting: uses the more conservative settling time to reduce the kinetic energy to a steady state value and is based on the maximum settling time (either w_s and t_{u_s} or w_s and t_{w_s}). w_s is the response value metric of interest in both cases as the intention is to determine the vertical flare height and not the horizontal flare distance.

Similarly, the acceleration (a) from trim during flare for the vertical velocity flare reduction setting is given by:

$$a_{t=t_{w_p}} = \frac{\delta_{s_{avail}} \times w_{p_{\delta_s}} + \delta_{\mu_{avail}} \times w_{p_{\delta_\mu}}}{t_{w_p}}, \tag{27}$$

where $w_{p_{\delta_s}}$ and $w_{p_{\delta_\mu}}$ are the peak w values in the δ_s and δ_μ step responses, respectively. $\delta_{s_{avail}}$ and $\delta_{\mu_{avail}}$ are defined as the difference between the maximum control input available and the current control input where $\delta_{s_{max}} = 1$ and $\delta_{\mu_{max}} = 0.0873$ rad (5°) as shown in Algorithm 1.

Algorithm 1 Flare controls determination

Require: flareHeightFlag, δ_s, $\delta_{s_{max}}$, δ_μ, $\delta_{\mu_{max}}$
  if flareHeightFlag = 0 **then**
    $\delta_{s_{flare}} \leftarrow 0$
    $\delta_{\mu_{flare}} \leftarrow 0$
  else if flareHeightFlag = 1 **then**
    $\delta_{s_{flare}} \leftarrow (\delta_{s_{max}} - \delta_s)$
    $\delta_{\mu_{flare}} \leftarrow (\delta_{\mu_{max}} - \delta_\mu)$
  end if

A value of 5° for $\delta_{\mu_{max}}$ was chosen as this allows for a total available deflection of 10° (5° upwards and 5° downwards), where a downward deflection is defined as negative. It has been assumed that the aerodynamic and control derivatives of the parafoil and eVTOL payload system do not change within the 10° rigging angle deflection range.

For the kinetic energy reduction flare setting, it is necessary to first determine the maximum settling time from either the u or w response to the combined control inputs. If this occurs in the u response, the acceleration is given by:

$$a_{t=t_{u_s}} = \frac{\delta_{s_{avail}} \times w_{s_{\delta_s}} + \delta_{\mu_{avail}} \times w_{s_{\delta_\mu}}}{t_{u_s}}, \tag{28}$$

or if it occurs in the w response, the acceleration is

$$a_{t=t_{w_s}} = \frac{\delta_{s_{avail}} \times w_{s_{\delta_s}} + \delta_{\mu_{avail}} \times w_{s_{\delta_\mu}}}{t_{w_s}}. \tag{29}$$

In all cases, it is the vertical {I} acceleration of interest and thus the w velocity is used for determining the change in velocity from trim. Note that $\delta_{s_{avail}}$ and $\delta_{\mu_{avail}}$ are always ≥ 0 and result in values of u_p, w_p, u_s, and δ_s that are ≤ 0.

Therefore, the flare height is calculated by

$$h_{flare} = |v_z| t + \frac{1}{2} a t^2 \tag{30}$$

where v_z is the vertical velocity in {I} obtained from the nonlinear model and t is the value of time corresponding to the flare setting chosen (peak velocity reduction or kinetic energy reduction).

Note that this method of calculating the flare height assumes a constant acceleration and thus the areas under the curve in Figure 8 are represented as a triangle. It can be seen that this triangle area approximates the area under the plot for the peak times and values relatively accurately but inaccurately captures the area for the settling times and values. As such, the settling kinetic energy reduction setting is erroneous due to susceptibility to wind shear and inaccuracies in determining the acceleration. An alternative and more accurate method to determine the flare height would be to integrate the area under the w

curve using the cumulative trapezium rule method. Indeed this method will be used in Section 3.3.3 to determine the horizontal distance travelled during flare.

3.2.2. Simulink Implementation

Figure 9 shows the Simulink implementation of the flare controller. A flare activation latch is employed in the model such that the flare controls remain activated from the first instance to the completion of the simulation when $h \leq 0$ m. Referring to (30) it can be seen that this is necessary as v_z reduces during flare, thereby decreasing the height required. The flare controls are added to the commanded controls such that the inner loop system acts in conjunction with the outer loop IPI-targeting system. If the IPI-targeting system is disabled, the inner-loop flare control system continues to operate providing that the control system is activated.

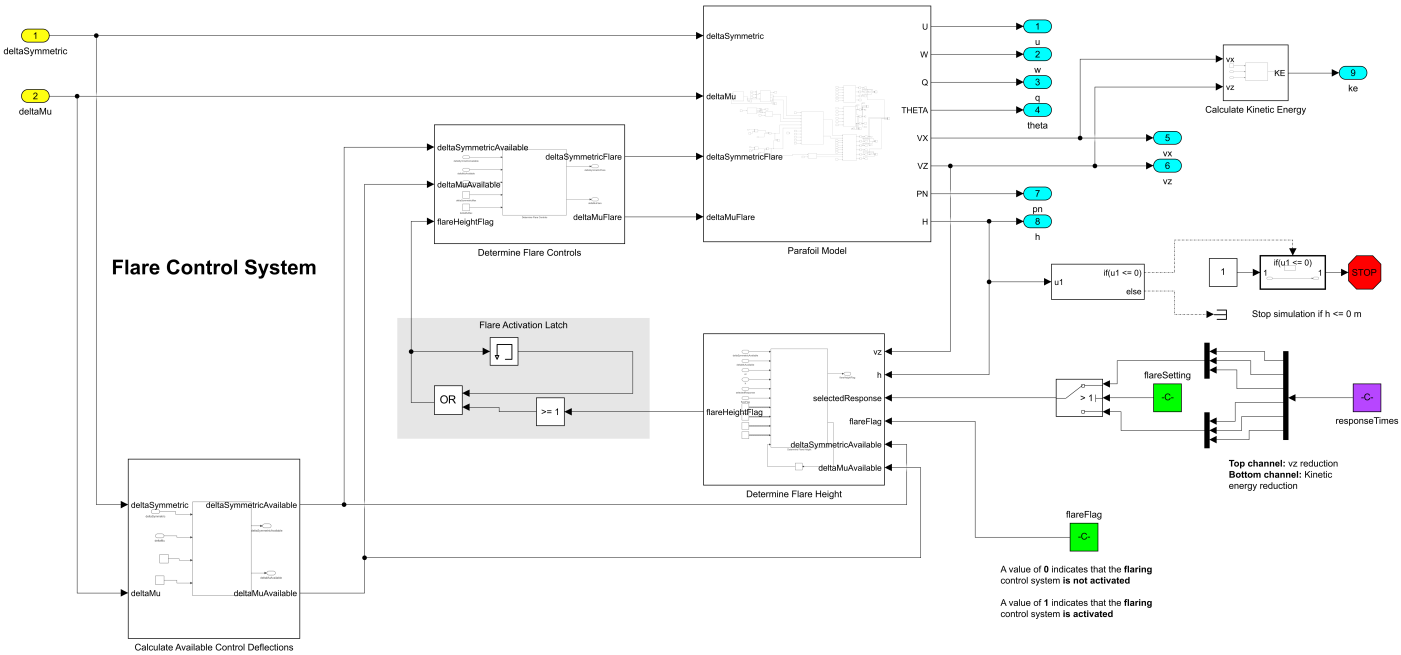

Figure 9. Simulink implementation of inner-loop flare controller.

3.3. Outer-Loop IPI-Targeting Control System

3.3.1. IPI Generation and Guidance Method

The first stage of the IPI-targeting control system guidance is the creation of the desired IPI. Once again using the assumption that $u \approx v_x$ and $w \approx v_z$ because θ is negligibly small, the desired IPI is calculated using the trim values of u and w by

$$P_{N_{land}} = \frac{h_{land} - c_{glide\ slope}}{m_{glide\ slope}}, \tag{31}$$

where $m_{glide\ slope} = -w_0/u_0$, $c_{glide\ slope} = h_0$, $h_{land} = 0$, h_0 is the trim height and $P_{N_{land}}$ is the desired IPI given that an initial P_N of 0 m is used. Thus, in zero wind and turbulence conditions, the parafoil and eVTOL system would glide directly to the ground and land at the desired IPI with the only landing error caused by the variable air density throughout the flight. However, in reality, both wind shear and turbulence cause the system to deviate significantly from the desired glide slope and land away from the desired IPI. As such, a path-following/IPI-targeting control system is required.

The path-following method involves following the glide slope locus using cross-track error, along-track error, and angle error. However, in path following, time is not a tracked variable and thus the future positions of the system over a short distance must be estimated,

leading to large error. An improved approach is to use a line-of-sight (LOS) method to aim the system velocity vector towards the desired IPI. This method uses the ratio of w/u to determine the LOS angle, which was shown to have a maximum error of 10.427% when comparing the linear to nonlinear system for wind conditions of 0 m/s and 5 m/s and heights of 100 m and 500 m in Figures 5–7. Furthermore, predicting the future LOS angle involves using the full horizontal and vertical distances to the desired IPI, thereby reducing the error in comparison to path following.

3.3.2. Standard Line-of-Sight Model Predictive Controller

Figure 10 shows the standard LOS guidance method. The flight path angle (λ) and LOS angle (θ_{LOS}) are defined as

$$\lambda = \tan^{-1}\left(\frac{w}{u}\right), \qquad \theta_{LOS} = \tan^{-1}\left(\frac{h_{ref}}{P_{N_{ref}}}\right). \tag{32}$$

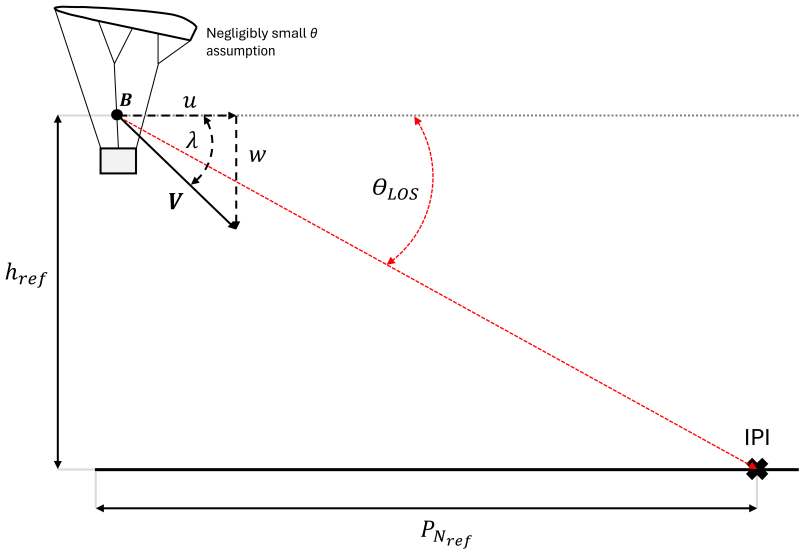

Figure 10. Standard longitudinal line-of-sight guidance method.

Because the linear system outputs u and w, and the error between the nonlinear and linear system are relatively small for the ratio of w/u, the linearised state space representation of the system is used in the MPC cost function as will be described later in this section.

In MPC, the optimum control inputs (u) over a prediction horizon (p) are found to minimise cost functions C_i as the sum

$$J = \sum_{i=k}^{k+p} C_i. \tag{33}$$

The summation from $i = k$ to $k + p$ denotes the receding horizon method of MPC. The controller starts at $k = 1$ at $t = 0$ and determines the control input that minimises the cost function over the specified prediction horizon. A prediction horizon (p) of two results in three stages (σ_{num}) (from k = 1 to (p+2) = 3 stages). This control is applied and the nonlinear system is simulated with this control input for a time equal to T_p. The process is repeated at $k = 2$ at $t = T_p$, $k = 3$ at $t = 2T_p$ and so forth.

From Figure 10, the target impact cost function is given by:

$$J = \sum_{i=k}^{k+p} \left[\theta_{LOS_{ref}} - \tan^{-1}\left(\frac{w}{u}\right)\right]^2 + {\delta_s}^2, \tag{34}$$

where the magnitude of δ_s is included in the cost function to penalise its use and therefore predominately uses δ_μ for IPI targeting. The predominant use of a single control was shown to reduce the overprediction of the required control input in preliminary simulations. Recall that the linearised system from trim conditions is used for MPC prediction. The cost function is applied across all stages, with the flare controller effectively overwriting the commanded values by the MPC controller once it is activated.

The reference LOS values ($\theta_{LOS_{ref}}$) are generated at each iteration of the MPC controller using a constant horizontal and vertical velocity in {I} assumption which is valid for sufficiently small stage prediction times (T_p). Algorithm 2 shows the process used to generate the reference LOS values.

The absolute values of the reference h and P_N have been used in Algorithm 2 to account for an overshoot in which $P_{N_{predicted}} > P_{N_{land}}$. In this situation, the optimum control is clearly to apply full brakes as this both reduces landing error and performs the flare manoeuvre. Referring to the cost function in (34), it can be seen that in the event of a sustained overshoot, $|\theta_{LOS_{ref}}|$ is positive and reduces in magnitude indicating that the cost is minimised by reducing the $\tan^{-1}(w/u)$ term. The step responses in Figures 5–7 show that applying full brakes and upward rigging angle tilt results in a similar speed reduction in u and w. However, u is typically greater than w in most wind conditions analysed. Therefore, $\tan^{-1}(w/u)$ is minimised in the event of an overshoot by applying full brakes and upward rigging angle tilt. In reality, this overshoot scenario rarely occurs as the flare control system is activated at a height at which the $P_{N_{land}} > P_{N_{predicted}}$, although it may occur in strong wind and turbulence conditions.

Algorithm 2 Prediction of $\theta_{LOS_{ref}}$ for standard LOS guidance method

Require: $P_N, h, \sigma_{num}, v_x, v_z, T_p$ ▷ σ_{num} is the number of stages

$P_{N_{predicted}} \leftarrow \left[P_N, \mathbf{0}_{1\times(\sigma_{num}-1)}\right]$
$h_{predicted} \leftarrow \left[h, \mathbf{0}_{1\times(\sigma_{num}-1)}\right]$
for $i \leftarrow 2$ to σ_{num} **do**
    $P_{N_{initial}} \leftarrow P_{N_{predicted_{i-1}}}$
    $h_{initial} \leftarrow h_{predicted_{i-1}}$
    $P_{N_{predicted_i}} \leftarrow P_{N_{initial}} + v_x \times T_p$
    $h_{predicted_i} \leftarrow h_{initial} + v_z \times T_p$
end for
for $i \leftarrow 1$ to σ_{num} **do**
    $\theta_{LOS_i} \leftarrow \tan^{-1}\left(\frac{|h_{predicted_i} - h_{land}|}{|P_{N_{land}} - P_{N_{predicted_i}}|}\right)$
end for

The guidance is invoked by solving the following nonlinear program:

$$\begin{aligned} &\min_{\boldsymbol{x}_k \to \boldsymbol{x}_{(k+p)}, \boldsymbol{u}_k \to \boldsymbol{u}_{(k+p)}} \sum_{i=k}^{k+p} J_i(x_i, u_i) \\ &\text{subject to: } \begin{cases} 0 < \delta_{s_i} \\ \delta_{s_i} < 1 \\ -0.0873 < \delta_{\mu_i} \\ \delta_{\mu_i} < 0.0873 \end{cases} \\ &\text{where: } J_i = \left\{ \left[\theta_{LOS_{ref_i}} - \tan^{-1}\left(\frac{w_i}{u_i}\right)\right]^2 + {\delta_{s_i}}^2 \right. \\ &\text{with: } \begin{cases} \boldsymbol{x}_0 = \boldsymbol{x}_{init} \\ \boldsymbol{u}_0 = [0, 0] \end{cases} \end{aligned} \tag{35}$$

where the optimum control inputs are determined using the interior-point algorithm called by the MATLAB `fmincon` function in the `nlmpcmove` function. The linearised state-space system generated from the trim conditions is used in the prediction stage and is initialised with the nonlinear model outputs at each iteration. This process will be explained in Section 3.4.

A trade-off exists between controller performance and computational cost when choosing the prediction time and horizon. A prediction horizon of one (two stages) resulted in a reactive oscillatory control method as shown in Figure 11.

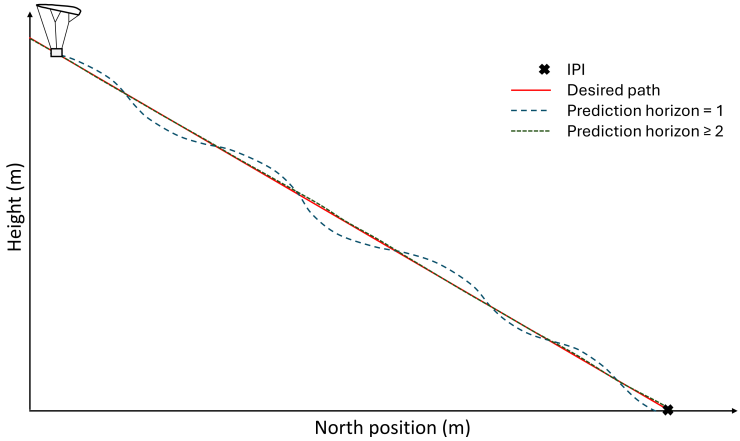

Figure 11. Relationship between prediction horizon and IPI-targeting behaviour of a parafoil and eVTOL payload system.

A prediction horizon of two (three stages) was found to be the minimum prediction horizon that resulted in a smooth IPI targeting. Additionally, a constant velocity assumption was made in predicting LOS reference values leading to the prediction time being limited to one in which the u and w velocities remained approximately constant. Furthermore, non-minimum phase behaviour is present in the u step response as visible in Figure 8, which lasts for ≈ 0.4 s. Hence, a stage prediction time of 0.45 s was chosen resulting in a prediction time of 0.90 s. Table 5 summarises the controller parameters.

Table 5. Parafoil and eVTOL payload system nonlinear model predictive controller parameters.

Stage Prediction Time (T_p)	Prediction Horizon (p)	Number of Stages (σ_{num})	Prediction Time (s)
0.45	2	3	0.9

A clear disadvantage of the standard LOS method is that the horizontal flare distance is not accounted for. The controller simply aims for the IPI using the nonlinear model predictive controller and at a condition-dependent height, the flare control system is activated. Thus the system may drift off course in the final stage of descent. This issue can be resolved by using a novel adaptive LOS method in which the target the system aims for accounts for the horizontal flare distance and is updated at each iteration of the model predictive controller. The design and implementation of this adaptive LOS model predictive controller are described in the proceeding Section.

3.3.3. Adaptive Line-of-Sight Model Predictive Controller

Consider the step response of the linear system shown in Figure 8. Once again using the small θ assumption and scaling property of LTI systems, the horizontal flare distance for peak vertical velocity reduction (x_{flare,t_p}) is given by:

$$x_{flare,t_p} = \delta_{s_{avail}} \times x_{flare,t_{p_{\delta_s}}} + \delta_{\mu_{avail}} \times x_{flare,t_{p_{\delta_\mu}}}, \tag{36}$$

where $x_{flare,t_{p_{\delta_s}}}$ and $x_{flare,t_{p_{\delta_\mu}}}$ represent the horizontal flare distances calculated from the u response resulting from a unit δ_s control input (u_{δ_s}) and a unit δ_μ control input (u_{δ_μ}), respectively. $x_{flare,t_{p_{\delta_s}}}$ and $x_{flare,t_{p_{\delta_\mu}}}$ are calculated by integrating the u step response:

$$x_{flare,t_{p_{\delta_s}}} = \int_{t'=0}^{t'=t_p} u_{\delta_s}\, dt', \qquad x_{flare,t_{p_{\delta_\mu}}} = \int_{t'=0}^{t'=t_p} u_{\delta_\mu}\, dt', \tag{37}$$

which is accomplished using the cumulative trapezium method.

Similarly, the horizontal flare distance for kinetic energy reduction (x_{flare,t_s}) is given by:

$$x_{flare,t_{s_{\delta_s}}} = \int_{t'=0}^{t'=t_s} u_{\delta_s}\, dt', \qquad x_{flare,t_{s_{\delta_\mu}}} = \int_{t'=0}^{t'=t_s} u_{\delta_\mu}\, dt' \tag{38}$$

Clearly, the horizontal flare distance is a function of the available control inputs and changes throughout the descent as shown in Figure 12.

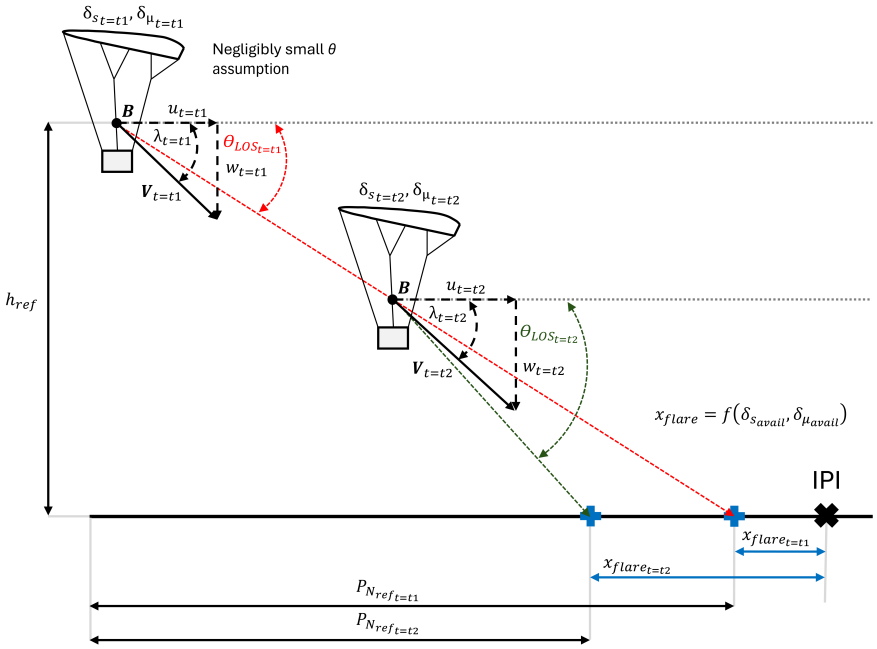

Figure 12. Adaptive longitudinal line-of-sight guidance method.

To account for this change in horizontal flare distance at each iteration of the MPC loop, $P_{N_{land}}$ is corrected at each iteration of the MPC loop by:

$$P_{N_{land,corrected}} = P_{N_{land}} - x_{flare}. \tag{39}$$

This process for the peak vertical velocity reduction flare method is shown in Algorithm 3. The kinetic energy reduction adaptive LOS guidance method formulation is equivalent. The controller parameters as shown in Table 5 remain unchanged for the adaptive LOS method.

Algorithm 3 Prediction of $\theta_{LOS_{ref}}$ for adaptive LOS guidance with peak vertical velocity reduction flare method

Require: P_N, h, σ_{num}, v_x, v_z, T_p, $\delta_{s_{avail}}$, $\delta_{\mu_{avail}}$, $x_{flare,t_{p_{\delta_s}}}$, $x_{flare,t_{p_{\delta_\mu}}}$

$P_{N_{predicted}} \leftarrow \left[P_N, \mathbf{0}_{1\times(\sigma_{num}-1)}\right]$
$h_{predicted} \leftarrow \left[h, \mathbf{0}_{1\times(\sigma_{num}-1)}\right]$
for $i \leftarrow 2$ to σ_{num} **do**
    $P_{N_{initial}} \leftarrow P_{N_{predicted_{i-1}}}$
    $h_{initial} \leftarrow h_{predicted_{i-1}}$
    $P_{N_{predicted_i}} \leftarrow P_{N_{initial}} + v_x \times T_p$
    $h_{predicted_i} \leftarrow h_{initial} + v_z \times T_p$
end for
$x_{flare,t_p} \leftarrow \delta_{s_{avail}} \times x_{flare,t_{p_{\delta_s}}} + \delta_{\mu_{avail}} \times x_{flare,t_{p_{\delta_\mu}}}$
$P_{N_{land,corrected}} \leftarrow P_{N_{land}} - x_{flare,t_p}$
for $i \leftarrow 1$ to σ_{num} **do**
    $\theta_{LOS_i} \leftarrow \tan^{-1}\left(\frac{|h_{predicted_i} - h_{land}|}{|P_{N_{land,corrected}} - P_{N_{predicted_i}}|}\right)$
end for

3.4. Complete Control System Layout

The full control system flow diagram is presented in Figure 13. It can be seen that the nonlinear model predictive control system acts outside of the flare control system. Therefore, it could be easily replaced with alternatives such as a PID if computational power is limited. This highlights a clear advantage of not implementing a terminal velocity/kinetic constraint in the model predictive controller. The inner-loop flare control system is a bang-bang control system with a latch to keep the flare controls deployed once activated, as previously described in Section 3.2.2.

The MPC state function as required in the nonlinear MPC prediction step requires both the state-space representation of the system and the trim values of the states as shown in Figure 13. Thus, the system dynamics in the MPC prediction step are calculated using

$$\begin{aligned} \dot{\boldsymbol{x}} &= \boldsymbol{A}(\boldsymbol{x} - \boldsymbol{x}_{trim}) + \boldsymbol{B}(\boldsymbol{u} - \boldsymbol{u}_{trim}) \\ \boldsymbol{x} &= [u,\ w,\ q,\ \theta]^T \\ \boldsymbol{u} &= [\delta_s,\ \delta_\mu]^T. \end{aligned} \tag{40}$$

Monte Carlo simulations were used to test the performance of the control system using the various IPI-targeting and flare settings as described in the following section.

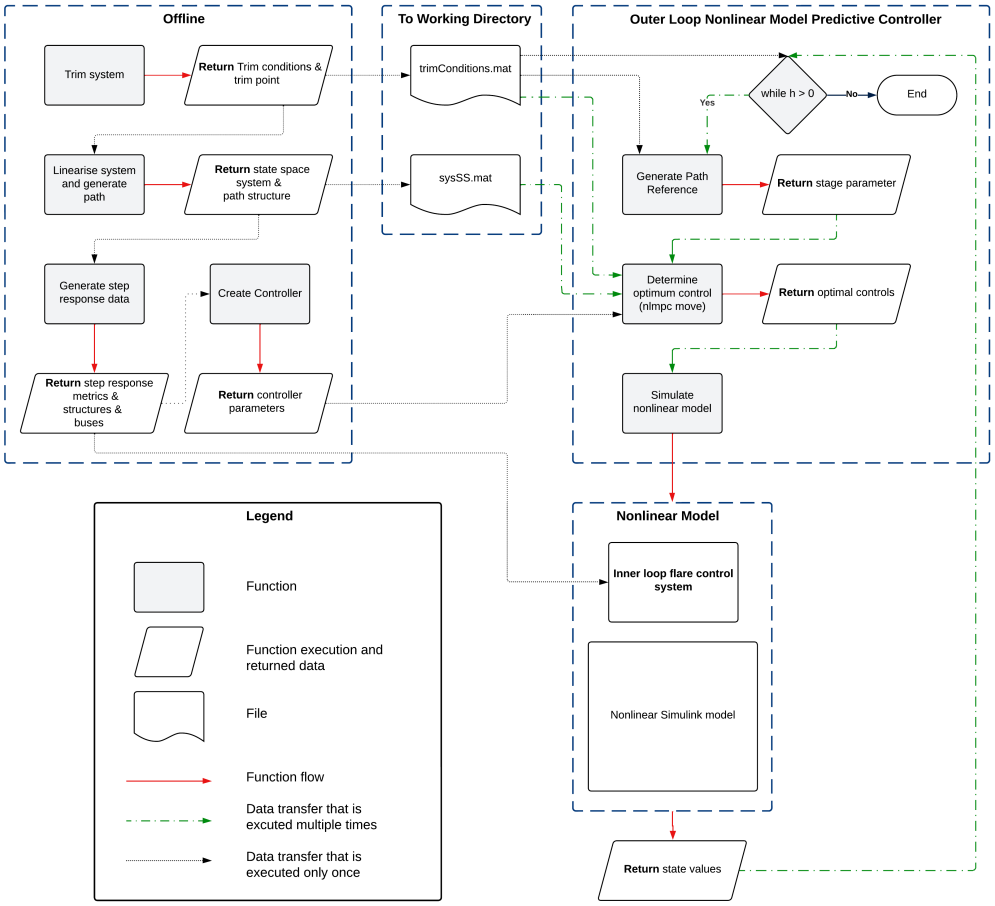

Figure 13. Full control system architecture.

3.5. Monte Carlo Simulation Setup

To test the controller performance in realistic conditions, three sources of variation were added as shown below.

1. Wind shear.
2. Dryden wind turbulence in the u and w directions.
3. Parameter uncertainty.

Wind shear and Dryden wind turbulence were implemented as previously described in Section 2.8. Random noise seeds using values in the range of $[1, 1000]$ were used to generate different turbulence profiles in each simulation.

Additionally, parameter uncertainty was added to the system mass (m), the displacement vector between the body axes centre and the parafoil axis centre ($\boldsymbol{r}_{BM}$), and the control derivatives. A random value for m centered around the nominal mass of 2600 kg with a standard error equal to 3% of the nominal value was generated at the initialisation of each simulation. This standard deviation corresponds to 78 kg, which is approximately the mass of one passenger. Similarly, random values for the entries in $\boldsymbol{r}_{BM}$ were generated in the same manner as for m with a standard error equal to 5% of the nominal value used. Randomising both m and $\boldsymbol{r}_{BM}$ varies the forces and moments on the system without causing the natural modes to become unstable. The aerodynamic derivatives in Table 3 were not varied as doing so may lead to natural mode instability and unrealistic behaviour. Furthermore, the purpose of the Monte Carlo simulations in this study is to test the robustness of the controller to the external environment and control derivative uncertainties, and not aerodynamic derivative uncertainties.

The control derivatives of $C_{D_{\delta_s}}$, $C_{L_{\delta_s}}$, $C_{D_{\delta_\mu}}$, and $C_{L_{\delta_\mu}}$ were randomised using a standard error equal to 2.5% of their nominal values. This value was chosen as it resulted in a

maximum $C_{L_{control}}/C_{D_{control}}$ variation of 5% when the standard error is equal to one standard deviation. Table 6 shows the Monte Carlo simulations matrix.

Table 6. Parafoil and eVTOL payload system Monte Carlo simulations matrix. "N" represents none, "S" represents standard, "A" represents adaptive, "KE" represents kinetic energy reduction, and "VV" represents vertical velocity reduction.

ID	Flare Mode	LOS Guidance	Wind Speed at 6 m (m/s)	Initial Heights (m)	Wind Shear	Dryden Wind Turbulence	Parameter Uncertainty	Num. Simulations
1A	N	S	[0, 1, 2, 3, 4, 5]	[100, 300, 500]	✓	✓	✓	50 × 18
1B	N	N	[0, 1, 2, 3, 4, 5]	[100, 300, 500]	✓	✓	✓	50 × 18
2A	VV	S	[0, 1, 2, 3, 4, 5]	[100, 300, 500]	✓	✓	✓	50 × 18
2B	N	N	[0, 1, 2, 3, 4, 5]	[100, 300, 500]	✓	✓	✓	50 × 18
3A	KE	A	[0, 1, 2, 3, 4, 5]	[100, 300, 500]	✓	✓	✓	50 × 18
3B	N	N	[0, 1, 2, 3, 4, 5]	[100, 300, 500]	✓	✓	✓	50 × 18

Note that the Monte Carlo simulation loop includes the simulation of both the controlled and uncontrolled system as represented by "A" and "B" in the ID column of Table 6. Using this method, the turbulence profile and parameter uncertainty values are the same for both the controlled and uncontrolled systems in the same simulation loop. This process is illustrated in Figure 14.

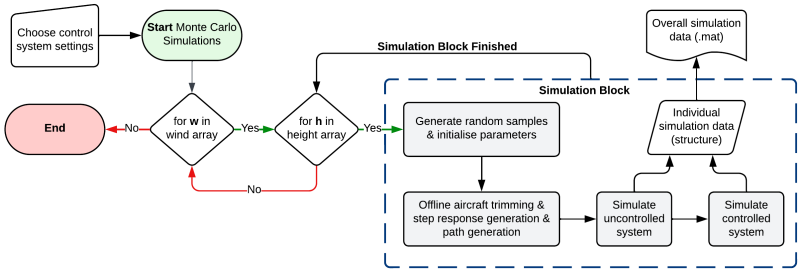

Figure 14. Monte Carlo simulation flowchart.

The philosophy used is to test the vertical velocity reduction flare setting with the standard LOS guidance system as in this control system the horizontal flare distance is not accounted for. Using the vertical velocity reduction flare setting minimises the time spent in flaring and thereby minimises landing error. Similarly, the kinetic energy reduction flare setting is tested with the adaptive LOS guidance system as the horizontal flare distance is considered in the guidance. Therefore, the time spent in flaring can be maximised and is set to the time required for a steady state reduction in kinetic energy.

The simulations were carried out using MATLAB R2023a on a desktop with 16 GB of RAM and an Intel® Core™ i5-8265U CPU @ 1.60 GHz (base)/1.80 GHz (turbo) processor (Santa Clara, CA, USA).

4. Results and Discussion

4.1. Overview

Results shows that the absolute landing error as defined by $\left|P_{N_{land}} - P_{N_{IPI}}\right|$ is skewed to the right in the controlled system results but normally distributed in the uncontrolled system results. As such, the median (50th percentile) and interquartile range (75th–25th percentile) were used to assess the performance of the control system as opposed to the mean and standard deviation. All median and interquartile range (IQR) values listed in this chapter are from Appendix A.1, Tables A1–A3.

In Section 1, a criterion was defined in which a vertical impact velocity of at most 8 m/s is required to reduce the likelihood of occupant spinal injury to less than 10% in a

generic eVTOL aircraft. The results in Appendix A.1, Tables A1–A3 show that the median landing vertical velocity in all simulations with the flare control system activated was less than 8 m/s thereby achieving this criterion. On the contrary, more than 62% of all median landing vertical velocities exceeded 8 m/s in the uncontrolled system.

4.2. Landing and Kinetic Energy Analysis

4.2.1. Landing Error

Examining first the landing error variation with height in Figures 15–17, it can be seen that the effectiveness of the control systems increases with height. The degree of effectiveness can be regarded as the improvement in performance of the controlled system compared to the uncontrolled system. Consider the $h_0 = 100$ m case where both control systems with flaring activated perform worse than the uncontrolled system. Assuming a constant vertical descent velocity of 8.2 m/s, which was found to be relatively independent of initial height and nominal wind speed at 6 m and realistic flare heights of 11 m and 36 m for the vertical velocity (VV) reduction and kinetic energy (KE) reduction flare settings, respectively, only 10.9 s of control is possible in the VV reduction flare with standard LOS guidance case. This corresponds to 24 MPC prediction steps (T_p = 0.45 s). This stage prediction time is inadequate at $h_0 = 100$ m but performs well at $h_0 = 300$ m and $h_0 = 500$ m. Figure 4 shows that the wind shear gradient (dw_x/dh) is greater at 100 m than at 300 m and 500 m, leading to the system quickly deviating from trim. As such, it is likely that a smaller stage prediction time is required at lower initial heights to account for this quick deviation from trim. This phenomenon is amplified in the KE reduction flare with adaptive LOS results at h_0 = 100 m as only approximately 7.8 s of the control (17 MPC) steps are possible before the flare control system is activated.

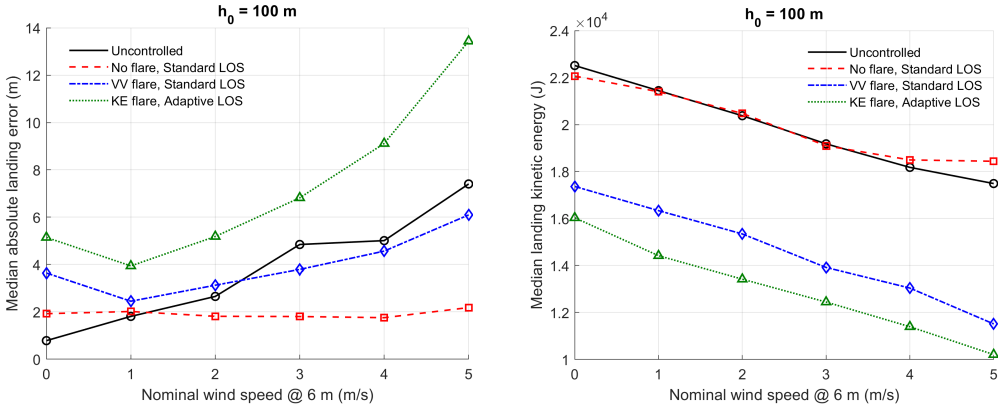

(**a**) Median absolute landing error, $h_0 = 100$ m (**b**) Median landing kinetic energy, $h_0 = 100$ m

Figure 15. Median absolute landing error and landing kinetic energy comparison for $h_0 = 100$ m.

Figure 18 below shows the landing error of the VV reduction flare setting with standard LOS guidance control system and KE reduction flare with adaptive LOS guidance control systems at a nominal wind speed at 6 m of 2 m/s.

Note that both controllers achieve their optimum landing error performance at this wind speed. It can be seen that the spread of landing positions is greater in the KE flare with adaptive LOS guidance system (IQR = [4.04, 5.1, 7.58] m at h_0 = [100, 300, 500] m) than in the VV flare with standard LOS guidance (IQR = [1.94, 2.13, 6.22] m at h_0 = [100, 300, 500] m). Indeed, the mean IQR across all nominal wind speeds at 6 m and initial heights is greater in the KE flare with adaptive LOS system (IQR = 8.79 m) than in the VV flare with standard LOS system (IQR = 7.66 m). This may be explained by the adaptive LOS guidance system using the linear step response of the system to determine both the horizontal and

vertical flare distances as opposed to just the vertical flare distance as in the standard LOS guidance method. It was shown in Table 4 that the error between the linear and nonlinear model is greater for the individual values of u and w than for the ratio of $\frac{w}{u}$. While the ratio of w/u is used in the LOS guidance, the individual values of u and w are used in the flare distance determination. Thus, the adaptive LOS system displays greater variation in landing positions as it is less robust to the variations in control derivatives.

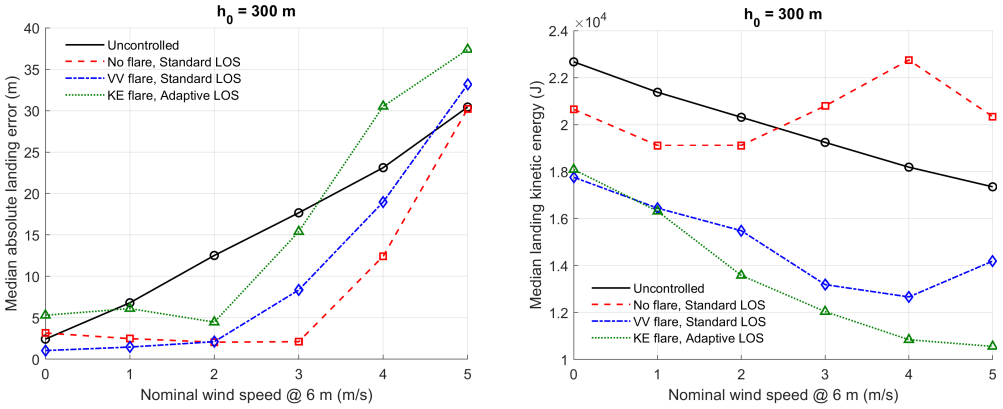

(**a**) Median absolute landing error, $h_0 = 300$ m (**b**) Median landing kinetic energy, $h_0 = 300$ m

Figure 16. Median absolute landing error and landing kinetic energy comparison for $h_0 = 300$ m.

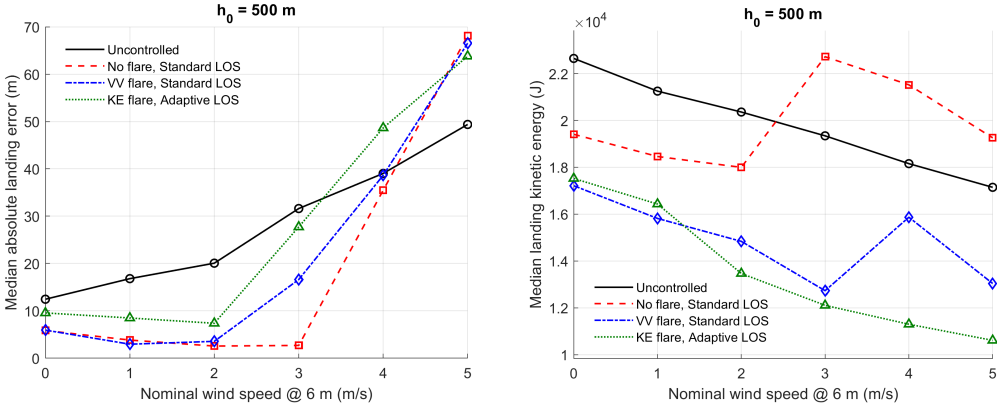

(**a**) Median landing kinetic energy, $h_0 = 500$ m (**b**) Median landing kinetic energy, $h_0 = 500$ m

Figure 17. Median absolute landing error and landing kinetic energy comparison for $h_0 = 500$ m.

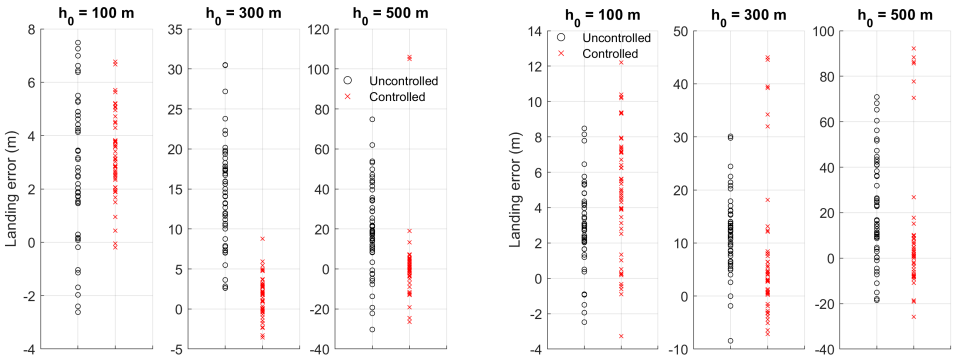

(**a**) (**b**)

Figure 18. Landing position of system with vertical velocity reduction flare setting and standard LOS guidance and system with kinetic energy reduction flare setting and adaptive LOS guidance. Nominal wind speed at 6 m of 2 m/s. (**a**) Vertical velocity reduction flare setting and standard LOS guidance. (**b**) Kinetic energy reduction flare setting and adaptive LOS guidance.

The open-loop (uncontrolled) system is shown to be robust to variations in m and $\boldsymbol{r}_{BM}$ by examining Figure 19. It can be seen that at h_0 = 100 m, the uncontrolled system lands at approximately the same position indicating that the trim values of u and w vary negligibly with variation in m and $\boldsymbol{r}_{BM}$. Median landing errors and IQRs of [0.784, 0.00393] m and [0.782, 0.00548] m, respectively, were recorded in Batches 2B and 3B (Table 6). As the initial height increases, the median landing error and IQR grows due to the prolonged effects of turbulence. Thus, it can be concluded that the open-loop system is robust to variations in m and $\boldsymbol{r}_{BM}$ with a standard error equal to 5% of their nominal values.

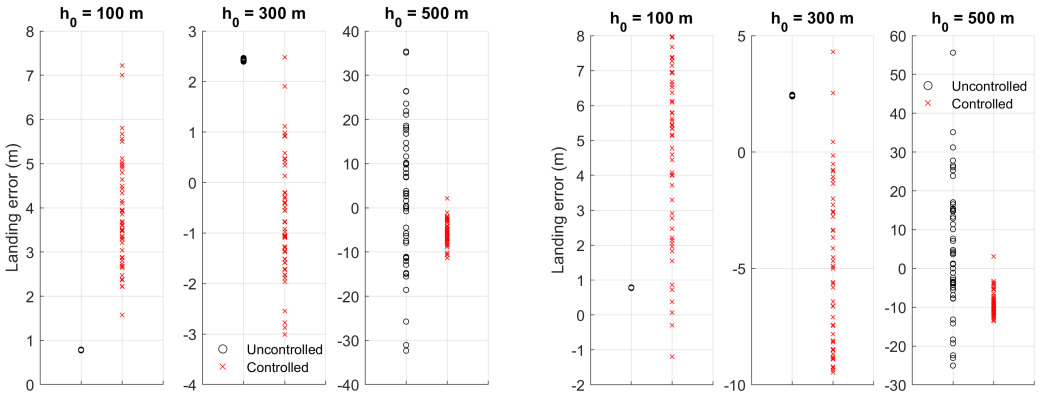

Figure 19. Landing position of system with vertical velocity reduction flare setting and standard LOS guidance and system with kinetic energy reduction flare setting and adaptive LOS guidance. Nominal wind speed at 6 m of 0 m/s. (**a**) Vertical velocity flare setting and standard LOS guidance. (**b**) Kinetic energy reduction flare setting and adaptive LOS guidance.

Returning to Figure 18, it is evident that although the median landing error decreases with the use of a control system, the maximum landing error occurred in the controlled systems. Table 7 shows the control derivative values for the maximum error cases at $h_0 = 500$ m. The worst-performing cases correspond to the simulations in which the $C_{Lcontrol}/C_{Dcontrol}$ ratio approaches or exceeds the maximum intended variation of 5% from its nominal value. The same is true for all wind conditions and initial heights. Therefore, it can be concluded that the closed-loop system is not robust to large variations in the control derivatives from their nominal values.

Table 7. Values of control derivatives for maximum landing error cases of system with vertical velocity reduction flare setting and standard LOS guidance and system with kinetic energy reduction flare setting and adaptive LOS guidance at an initial height of 500 m and nominal wind speed at 6 m of 2 m/s.

Parameter	Nominal Values	VV Flare, Standard LOS	KE Flare, Adaptive LOS
Landing error (m)	-	106.06	92.15
$C_{L_{\delta_s}}$	0.4	0.3827	0.3909
$C_{D_{\delta_s}}$	0.21	0.2116	0.2203
$C_{L_{\delta_\mu}}$ (/rad)	3.95	3.8202	3.9712
$C_{D_{\delta_\mu}}$ (/rad)	2	2.0752	2.105
% variation from nominal $\frac{C_{L_{\delta_s}}}{C_{D_{\delta_s}}}$ ratio	-	5.05	6.84
% variation from nominal $\frac{C_{L_{\delta_\mu}}}{C_{D_{\delta_\mu}}}$ ratio	-	6.79	4.48

A significant trend seen in Figures 15–17 is that the control system with standard LOS outperforms the control system with adaptive LOS with regard to landing error. It was hypothesised that the system would drift off course once the flare control system was engaged as the standard LOS guidance system does not account for the horizontal flare distance. Although this does occur, the effects are minimal as the system with flare disabled and standard LOS guidance (i.e., flies directly towards the IPI without flaring) has a landing error comparable to the system with VV reduction flaring enabled and standard LOS guidance. This can be explained by examining Figure 20. Coincidentally, the effects of wind shear result in the optimum MPC control near the ground being one that slows the system down. As the wind reduces due to wind shear, the ground speed of the system increases and thus symmetric brake deflection and an upward rigging angle tilt are required to slow the system down. Although full control deflections are not applied, a partial flare occurs as evidenced by the landing kinetic energy (LKE) being lower in the system with no flare and standard LOS guidance than in the uncontrolled system at nominal wind speeds at 6 m of less than 2.5 m/s. The flare manoeuvre may therefore be considered symbiotic with the LOS guidance in the terminal stages of landing. Note that the LKE in the system with no flare setting and standard LOS guidance is greater than the uncontrolled system at nominal wind speeds at 6 m of greater than 2.5 m/s as the robustness limit of the controller is met. This is discussed in the preceding section.

The relative under performance of the system with KE reduction flare setting and adaptive LOS guidance can be explained by the linear model over predicting the horizontal flaring distance. This can be confirmed by noting that the modal landing error is negative at low nominal wind speeds at 6 m in Appendix A.1, Figure A3. The step responses in Figures 5 and 6 show that the linear model over predicts the peak values of u and w. Consequently, the flare height is also over predicted leading to the actual distance travelled during flaring by the nonlinear model being less than the predicted distance by the linear model. Although this affects the landing error, it likely does not affect the minimisation of KE at landing as the conservative maximum settling time is used in the KE reduction flare setting.

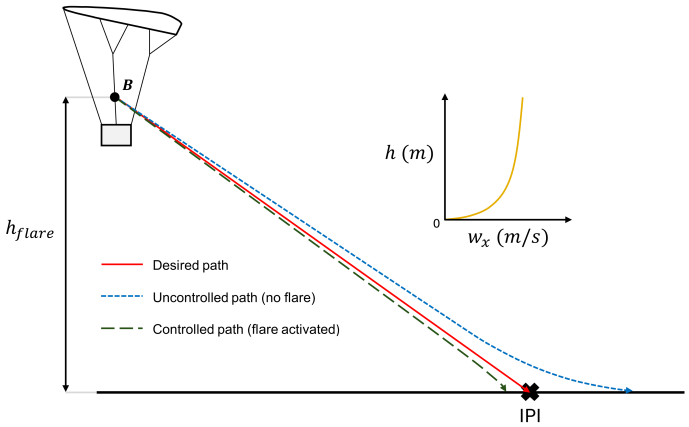

Figure 20. Comparison of system path loci during flaring with and without the flare control system activated.

In future work, an automatic gain correction step could be added in the offline controller phase by simulating the nonlinear model once to determine the step responses at trim and comparing this to the linear step responses. The gains that multiply the linear u and w step responses could then be defined as:

$$K_u = \frac{u_{peak_{nonlinear}}}{u_{peak_{linear}}}, \qquad K_w = \frac{w_{peak_{nonlinear}}}{w_{peak_{linear}}}. \tag{41}$$

4.2.2. Kinetic Energy

As expected, the LKE in Figures 15–17 is predominantly lower in the system with the KE reduction flare setting than in the system with the VV reduction flare setting. A decrease in LKE with an increase in wind speed is observed in the controlled systems with flaring activated and the uncontrolled system. This can be explained by the trim x velocities in {I} (i.e., the ground speed) being lower at higher nominal wind speeds at 6 m.

The system with the VV reduction flare setting and adaptive LOS guidance outperforms the system with the KE reduction flare setting at initial nominal wind speeds at 6 m of 0 m/s and 1 m/s at initial drop heights of 300 m and 500 m. Referring to the step response of the nonlinear system in Figures 5–7, it can be seen that a total velocity reduction of ≈6.02 m/s is possible if the time for a peak reduction in w is precisely met in comparison to a total velocity reduction of ≈4.25 m/s in the KE reduction (t_s) case. Thus, at low nominal wind speeds at 6 m with VV reduction flaring enabled, the system impacts the ground at a flaring time close to t_{w_p} leading to optimum flaring performance. However, at higher wind speeds, the differences between the nonlinear and linear systems are larger leading to an impact at a time greater than or less than t_{w_p}. The main advantage of the KE reduction flare setting is present in its robustness to deviations from the linear system. As the max settling time is used, deviations from this time result in negligible differences in KE reduction. The robustness of the KE setting is shown by a mean IQR of 1701 J across all nominal wind speeds at 6 m and initial heights in comparison to the mean IQR of 2140 J for the VV setting.

The superior robustness of the KE reduction flare setting is evident from the contour plots in Figure 21. The isolines for the KE reduction flare setting remain nearly perpendicular to the x-axis across all nominal wind speeds at 6 m, demonstrating that the control system's performance is relatively invariant to height. In contrast, the isolines for the VV reduction flare setting deviate significantly from perpendicularity to the x-axis at nominal wind speeds exceeding 3 m/s at 6 m, indicating that the robustness limit has been reached.

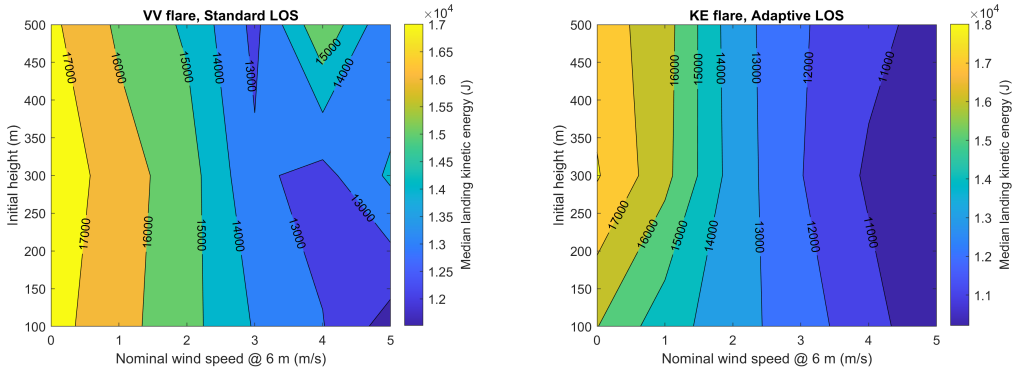

(**a**) (**b**)

Figure 21. Landing kinetic energy contour plots for system with vertical velocity reduction flare setting and standard LOS guidance and system with kinetic energy reduction flare setting and adaptive LOS guidance. (**a**) Vertical velocity reduction flare setting and standard LOS guidance. (**b**) Kinetic energy reduction flare setting and adaptive LOS guidance.

The system with no flare setting and standard LOS guidance was found to be sensitive to variations in the control derivatives leading to excessive control inputs being predicted at wind speeds greater than 2 m/s. As was shown in Figure 20, the optimum control input in high wind shear conditions is to apply breaking to prevent overshoot of the desired IPI. Figure 22 shows that this over prediction of the required control input results in the system landing short of the desired IPI in many cases. Consequently, in these cases, a negative control input was required near the ground to increase the ground speed of the system and

reduce landing error. This explains the increase in landing kinetic energy of the system at wind speeds greater than 2.5 m/s seen in Figures 15–17.

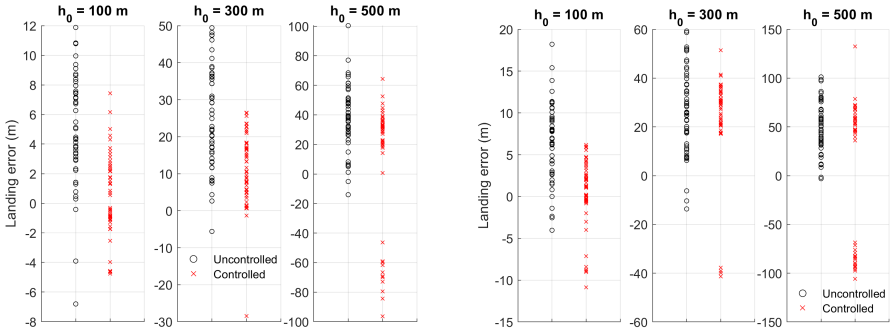

(**a**) Nominal wind speed at 6 m = 4 m/s (**b**) Nominal wind speed at 6 m = 5 m/s

Figure 22. Landing error of system with no flare setting and standard LOS guidance at nominal wind speeds at 6 m of 4 m/s and 5 m/s.

4.3. Controller Performance Limits

While the previous sections have provided an analysis of the control system robustness to wind shear, this section provides a graphical summary of the performance limits. The performance limit was defined based on the nominal wind speeds at 6 m in which the controlled system outperforms the uncontrolled system with regard to landing error and landing kinetic energy. Figure 23 presents the results. Table 8 shows the area of the simulation sample space in which the controlled system outperforms the uncontrolled system and Figure 24 shows the simulation sample space and performance limits.

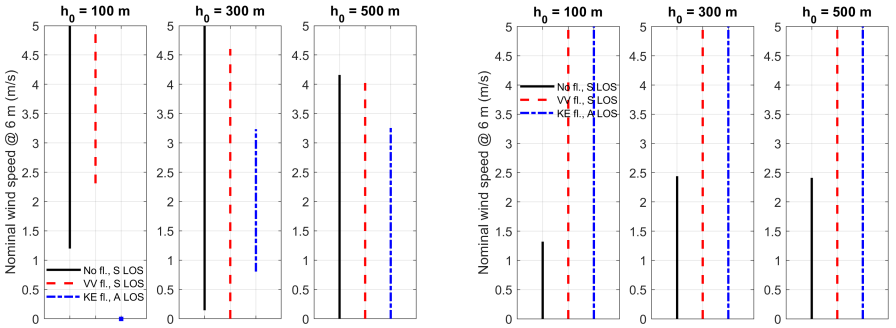

(**a**) Landing error (**b**) Landing kinetic energy

Figure 23. Performance limits of system with no flare setting and standard LOS guidance, system with kinetic energy reduction flare setting and standard LOS guidance, and system with vertical velocity reduction flare setting and adaptive LOS guidance.

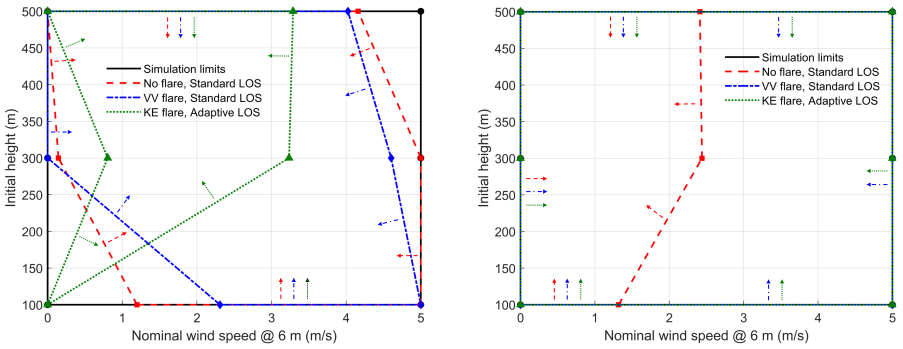

(**a**) Landing position error (**b**) Landing kinetic energy

Figure 24. Performance limits of controllers. The arrows point towards the area in which the controlled system has a lower median landing kinetic energy than the uncontrolled system.

Table 8. Percentage area of simulation sample space in which the controlled system outperforms the uncontrolled system.

Control System	Landing Error (%)	Landing Kinetic Energy (%)
No flare, Standard LOS	88.43	43.03
VV flare, Standard LOS	79.64	100
KE flare, Adaptive LOS	40.73	100

5. Conclusions

This paper presented the design and implementation of an inner-loop flare controller and an outer-loop MPC LOS guidance longitudinal control system for a six-DOF parafoil and eVTOL payload model. The inner-loop flare control included two settings: a VV flare setting, targeting peak velocity reduction during flaring, and a KE setting, focusing on the velocity reduction settling time. A standard outer-loop MPC LOS guidance method was developed where the system aimed for the desired point of impact and activated the flare control at a condition-dependent height above the ground. Additionally, an adaptive MPC LOS guidance system was created to dynamically adjust the landing point based on the predicted horizontal distance travelled during flaring at each timestep.

Flare activation significantly reduced landing KE and VV in all cases, with the KE flare setting providing the greatest reduction. The KE setting was also more robust due to its conservative use of maximum settling time, yielding a mean IQR of 1701 J across all nominal wind speeds at 6 m and initial heights in comparison to 2140 J for the VV setting.

The standard LOS guidance system outperformed the adaptive LOS system in terms of landing error across all heights and wind speeds. This was as expected for the system no-flare control and standard LOS guidance, as it targets the IPI throughout. However, the KE flare system with standard LOS guidance unexpectedly outperformed the adaptive system. The optimal MPC control, which accounted for wind shear, acted like a partial flare by reducing horizontal ground speed to prevent overshoot. It was found that the errors between the linear and nonlinear response led to the control system predicting a greater horizontal flare distance during flare, leading to the system falling short of the desired IPI in many cases.

Landing position error performance was reduced at nominal wind speeds at 6 m that are at least 3 m/s, and the system was found to be sensitive to changes in the control derivative lift-to-drag ratio at high wind speeds. Poor performance in simulations occurred when the control derivative lift-to-drag ratio deviated by more than 5% from nominal values, likely due to the system being tuned with nominal control derivatives. The non-minimum phase behaviour in the u step response is likely to deviate with changes in the control derivatives, which may require an increase in the value of T_p. Non-minimum phase behaviour that extends past the entire prediction horizon time will cause errors in the prediction of the w/u ratio from the linear model. At higher wind speeds, wind shear gradients rendered control inputs less effective, but kinetic energy reduction improved due to the lower trim horizontal ground speed caused by headwinds.

Author Contributions: Conceptualization, S.D., T.S., and J.F.W.; methodology, S.D.; software, S.D.; validation, S.D.; formal analysis, S.D.; investigation, S.D.; resources, S.D., T.S., and J.F.W.; data curation, S.D.; writing—original draft preparation, S.D.; writing—review and editing, T.S. and J.F.W.; visualization, S.D.; supervision, T.S. and J.F.W. All authors have read and agreed to the published version of the manuscript.

Funding: This research received no external funding.

Data Availability Statement: Some or all data, models, or codes that support the findings of this study are available from the corresponding author upon reasonable request.

Conflicts of Interest: The authors declare no conflicts of interest.

Abbreviations

The following abbreviations are used in this manuscript:

A LOS	Adaptive Line of sight
CG	Centre of gravity
DCM	Direction cosine matrix
DOF	Degree of freedom
DRI	Dynamic response index
eVTOL	Electric vertical take-off and landing
GNC	Guidance, navigation, and control
IPI	Initial point of impact
IQR	Interquartile range
KE	Kinetic energy
LKE	Landing kinetic energy
LOS	Line of sight
LTI	Linear time-invariant
MPC	Model predictive control
PID	Proportional–integral-derivative
S LOS	Standard line of sight

Appendix A

Appendix A.1. Tabulated Results

Table A1. Monte Carlo simulations results for system with no flare setting and standard LOS guidance and uncontrolled system.

Wind Speed at 6 m (m/s)	h_0 (m)	Abs. Landing Error (m) Median, IQR (Uncontrolled)	Abs. Landing Error (m) Median, IQR (Controlled)	Landing KE (J) Median, IQR (Uncontrolled)	Landing KE (J) Median, IQR (Controlled)	Landing Vert. Vel. (m/s) Median, IQR (Uncontrolled)	Landing Vert. Vel. (m/s) Median, IQR (Controlled)	% Landings with Vert. Vel. $>$ 8 m/s (Uncontrolled)	% Landings with Vert. Vel. $>$ 8 m/s (Controlled)
0	100	0.784, 0.00509	1.92, 1.07	22700, 1321	22066, 2902	−8.09, 0.157	−9.72, 3.13	76	64
0	300	2.42, 0.0183	3.16, 2.26	22600, 1246	20649, 2244	−8.08, 0.150	−8.49, 1.05	74	76
0	500	12.7, 13.5	5.85, 3.97	22700, 1456	19408, 1791	−8.09, 0.173	−8.04, 1.11	72	52
1	100	1.78, 1.98	2.01, 0.943	21400, 1225	21399, 2893	−8.2, 0.149	−9.59, 4.08	90	72
1	300	7.18, 6.03	2.48, 1.97	21400, 1245	19111, 2744	−8.21, 0.194	−8.7, 1.52	90	78
1	500	19.5, 19.6	3.83, 3.46	21400, 1382	18461, 3355	−8.19, 0.197	−8.42, 1.76	86	64
2	100	2.66, 2.47	1.81, 1.18	20500, 1043	20477, 3446	−8.33, 0.186	−9.72, 4.37	98	70
2	300	11.4, 7.17	2.05, 1.39	20300, 1766	19117, 2925	−8.31, 0.252	−9.36, 2.73	92	74
2	500	20.6, 21.5	2.56, 4.95	20500, 1549	17998, 3936	−8.33, 0.214	−8.13, 3.25	100	52
3	100	4.35, 2.65	1.8, 0.838	19100, 1437	19098, 3655	−8.41, 0.352	−8.77, 4.19	98	54
3	300	21.2, 18.5	2.11, 3	19000, 1237	20793, 4439	−8.41, 0.309	−9.2, 3.85	98	74
3	500	30.8, 41.4	2.69, 12.9	19300, 1698	22720, 8007	−8.4, 0.351	−10.4, 3.8	98	76
4	100	5.3, 4.61	1.75, 2.36	18200, 1699	18496, 4486	−8.59, 0.392	−8.74, 3.53	100	66
4	300	23.8, 20.8	12.4, 12.7	18200, 1303	22750, 3827	−8.51, 0.441	−10.1, 2.47	98	84
4	500	37.8, 23.6	35.5, 18.7	18400, 1513	21519, 5950	−8.64, 0.372	−9.47, 3.66	100	70
5	100	6.66, 6.31	2.18, 3.75	17400, 1617	18439, 7634	−8.74, 0.526	−9.02, 3.91	98	74
5	300	25.9, 26.1	30.2, 11.8	17100, 1520	20339, 2054	−8.7, 0.358	−10.5, 1.26	100	90
5	500	48.7, 35.6	68.1, 30.8	16800, 1876	19257, 7073	−8.63, 0.413	−9.59, 3.27	94	56

Table A2. Monte Carlo simulations results for system with vertical velocity reduction flare setting and standard LOS guidance and uncontrolled system.

Wind Speed at 6 m (m/s)	h_0 (m)	Abs. Landing Error (m) Median, IQR (Uncontrolled)	Abs. Landing Error (m) Median, IQR (Controlled)	Landing KE (J) Median, IQR (Uncontrolled)	Landing KE (J) Median, IQR (Controlled)	Landing Vert. Vel. (m/s) Median, IQR (Uncontrolled)	Landing Vert. Vel. (m/s) Median, IQR (Controlled)	% Landings with Vert. Vel. $>$ 8 m/s (Uncontrolled)	% Landings with Vert. Vel. $>$ 8 m/s (Controlled)
0	100	0.784, 0.00393	3.64, 1.91	22600, 1026	17367, 1338	−8.08, 0.122	−4.43, 0.423	82	0
0	300	2.43, 0.0213	1.04, 1.1	22700, 1418	17758, 1642	−8.09, 0.169	−5.42, 0.362	74	0
0	500	11.4, 11.7	5.93, 3.57	22900, 1299	17215, 1856	−8.11, 0.154	−5.72, 0.197	78	0
1	100	1.69, 1.41	2.45, 1.06	21400, 1429	16338, 1775	−8.2, 0.144	−4.48, 0.527	94	0
1	300	6.55, 3.4	1.46, 1.27	21400, 1176	16444, 1384	−8.18, 0.179	−5.45, 1.1	94	0
1	500	17.4, 23.9	2.95, 3.58	21400, 980	15817, 1882	−8.19, 0.185	−5.66, 0.599	94	0

Table A2. *Cont.*

Wind Speed at 6 m (m/s)	h_0 (m)	Abs. Landing Error (m) Median, IQR (Uncontrolled)	Abs. Landing Error (m) Median, IQR (Controlled)	Landing KE (J) Median, IQR (Uncontrolled)	Landing KE (J) Median, IQR (Controlled)	Landing Vert. Vel. (m/s) Median, IQR (Uncontrolled)	Landing Vert. Vel. (m/s) Median, IQR (Controlled)	% Landings with Vert. Vel. $>$ 8 m/s (Uncontrolled)	% Landings with Vert. Vel. $>$ 8 m/s (Controlled)
2	100	2.65, 2.93	3.13, 1.94	20300, 1391	15346, 1197	−8.33, 0.205	−4.62, 0.551	96	0
2	300	14.8, 7.8	2.11, 2.13	20600, 1494	15483, 1590	−8.33, 0.278	−4.98, 1	96	0
2	500	19.3, 23.3	3.56, 6.22	20100, 1657	14840, 2207	−8.32, 0.23	−5.23, 1.27	96	0
3	100	4.99, 3.67	3.79, 2.99	19100, 1719	13920, 1152	−8.42, 0.287	−4.66, 0.489	100	0
3	300	18.2, 9.4	8.35, 9.87	19500, 1162	13189, 2000	−8.48, 0.32	−4.06, 0.797	98	0
3	500	38.3, 28.2	16.6, 16.7	19400, 1249	12734, 2138	−8.44, 0.261	−4.04, 0.747	100	0
4	100	5.37, 5.78	4.57, 4.77	18300, 1188	13042, 1774	−8.55, 0.306	−4.72, 0.93	100	0
4	300	26.7, 16.1	19, 9.35	18400, 1443	12664, 4739	−8.47, 0.37	−4.58, 1.18	98	0
4	500	40.1, 22.7	38.6, 27.1	18000, 1642	15870, 4052	−8.53, 0.355	−5.34, 0.678	100	0
5	100	7.27, 6.94	6.1, 6.17	17300, 1643	11515, 1564	−8.59, 0.425	−4.51, 1.27	98	0
5	300	35, 17.5	33.2, 12.4	17300, 1267	14190, 2541	−8.59, 0.379	−5.49, 0.205	98	0
5	500	50.6, 29.1	66.5, 25.8	17400, 1773	13041, 3691	−8.71, 0.462	−5.54, 0.356	100	0

Table A3. Monte Carlo simulations results for system with kinetic energy reduction flare setting and adaptive LOS guidance and uncontrolled system.

Wind Speed at 6 m (m/s)	h_0 (m)	Abs. Landing Error (m) Median, IQR (Uncontrolled)	Abs. Landing Error (m) Median, IQR (Controlled)	Landing KE (J) Median, IQR (Uncontrolled)	Landing KE (J) Median, IQR (Controlled)	Landing Vert. Vel. (m/s) Median, IQR (Uncontrolled)	Landing Vert. Vel. (m/s) Median, IQR (Controlled)	% Landings with Vert. Vel. $>$ 8 m/s (Uncontrolled)	% Landings with Vert. Vel. $>$ 8 m/s (Controlled)
0	100	0.782, 0.00548	5.15, 4.32	22600, 1412	16033, 2162	−8.04, 0.169	−4.51, 0.352	62	0
0	300	2.42, 0.0222	5.3, 5.59	22600, 1518	18088, 3182	−8.08, 0.181	−6.36, 1.75	68	0
0	500	13, 14	9.56, 3.73	22600, 1515	17524, 2188	−8.08, 0.181	−6.49, 1.58	68	0
1	100	2.06, 1.55	3.94, 3.45	21300, 1706	14419, 1537	−8.17, 0.207	−4.33, 0.995	94	0
1	300	6.12, 6.5	6.11, 5.12	21400, 1289	16311, 3399	−8.17, 0.177	−4.98, 2.5	94	0
1	500	17, 16.5	8.49, 2.65	21300, 1113	16431, 2879	−8.17, 0.165	−6.76, 1.94	92	0
2	100	2.99, 2.06	5.18, 4.04	20300, 1377	13420, 1530	−8.32, 0.274	−4.65, 0.816	92	0
2	300	11.8, 7	4.47, 5.1	20100, 1608	13580, 2376	−8.32, 0.226	−4.66, 0.775	96	0
2	500	18.2, 30.7	7.37, 7.58	20400, 1255	13469, 2753	−8.34, 0.275	−5.07, 1.45	98	0
3	100	4.96, 4.02	6.82, 4.96	19300, 1123	12447, 1406	−8.47, 0.285	−4.72, 0.59	98	0
3	300	12.7, 11.5	15.4, 10.1	19300, 1186	12040, 998	−8.48, 0.301	−4.99, 0.461	98	0
3	500	26.8, 26	27.7, 21.3	19300, 1749	12109, 1239	−8.48, 0.375	−5.3, 0.738	98	0
4	100	5.77, 5.21	9.11, 4.43	18200, 1602	11396, 841	−8.52, 0.389	−5.19, 0.463	100	0
4	300	19.2, 12.9	30.5, 11.4	18100, 1723	10842, 777	−8.47, 0.309	−5.62, 0.415	96	0
4	500	38.3, 33.4	48.7, 24.4	18000, 1305	11303, 611	−8.58, 0.258	−5.97, 0.373	98	0
5	100	8.49, 6.41	13.4, 4.76	17500, 1442	10210, 931	−8.65, 0.509	−5.38, 0.443	94	0
5	300	29.3, 21.8	37.4, 14.2	17500, 1761	10558, 854	−8.63, 0.392	−6.1, 0.564	98	0
5	500	46.6, 43	63.8, 21	16900, 2036	10615, 961	−8.58, 0.395	−6.2, 0.308	98	0

Table A4. Linear correlation between landing error and landing velocity/kinetic energy for system with vertical velocity reduction flare setting and standard LOS guidance and system with kinetic energy reduction flare setting and adaptive LOS guidance.

Wind Speed at 6 m (m/s)	h_0 (m)	VV Flare, Standard LOS				KE Flare, Adaptive LOS			
		R^2 $V_{z_{land}}$	RMSE $V_{z_{land}}$	R^2 KE_{land}	RMSE KE_{land}	R^2 $V_{z_{land}}$	RMSE $V_{z_{land}}$	R^2 KE_{land}	RMSE KE_{land}
0	100	0.034	1.216	0.168	1.128	0.027	2.477	0.532	1.717
	300	0.017	1.175	0.049	1.156	0.552	2.33	0.493	2.476
	500	0.192	2.489	0.194	2.485	0.257	2.791	0.004	3.231
1	100	0.573	0.629	0.119	0.905	0.012	2.438	0.298	2.055
	300	0.836	0.793	0.199	1.751	0.332	5.454	0.451	4.947
	500	0.504	4.502	0.02	6.331	0.204	12.638	0.129	13.222
2	100	0.724	0.823	0.078	1.505	0.023	3.435	0.403	2.684
	300	0.816	1.077	0.011	2.494	0.039	12.96	0.268	11.308
	500	0.259	19.708	0.307	19.048	0.013	29.333	0.146	27.285
3	100	0.806	1.107	0.078	2.413	0.049	3.604	0.354	2.971
	300	0.295	5.7	0.293	5.709	0.112	9.617	0.019	10.11
	500	0.17	24.66	0.187	24.413	0.014	30.879	0.001	31.072
4	100	0.839	1.543	0.111	3.624	0.204	3.711	0.018	4.119
	300	0.002	11.556	0.128	10.799	0.296	10.339	0.125	11.525
	500	0.263	37.618	0.509	30.717	0.317	40.63	0.119	46.153
5	100	0.593	3.475	0.052	5.303	0.391	2.93	0.228	3.298
	300	0.201	22.199	0.403	19.185	0.139	11.287	0.005	12.13
	500	0.275	60.512	0.615	44.077	0.205	37.067	0.058	40.345
Average		0.411	11.155	0.196	10.169	0.177	12.44	0.203	12.814

Table A5. Performance limits of system with vertical velocity reduction flare setting and standard LOS guidance, system with kinetic energy reduction flare setting and adaptive LOS guidance and system with no flare setting and standard LOS guidance.

h_0 (m)	VV Flare, Standard LOS Wind Speed at 6 m Robustness Range (m/s)	KE Flare, Adaptive LOS Wind Speed at 6 m Robustness Range (m/s)	No Flare, Standard LOS Wind Speed at 6 m Robustness Range (m/s)
		Landing error	
100	[2.31, 5]	[0, 0]	[1.198, 5]
	[0, 0]	[0, 0]	[0, 0]
	[0, 0]	[0, 0]	[0, 0]

Table A5. *Cont.*

h_0 (m)	VV Flare, Standard LOS Wind Speed at 6 m Robustness Range (m/s)	KE Flare, Adaptive LOS Wind Speed at 6 m Robustness Range (m/s)	No Flare, Standard LOS Wind Speed at 6 m Robustness Range (m/s)
		Landing error	
300	[0, 4.603] [0, 0] [0, 0]	[0.805, 3.235] [0, 0] [0, 0]	[0.145, 5] [0, 0] [0, 0]
500	[0, 4.023] [0, 0] [0, 0]	[0, 3.288] [0, 0] [0, 0]	[0, 4.160] [0, 0] [0, 0]
		Kinetic energy	
100	[0, 5] [0, 0] [0, 0]	[0, 5] [0, 0] [0, 0]	[0, 1.320] [0, 0] [0, 0]
300	[0, 5] [0, 0] [0, 0]	[0, 5] [0, 0] [0, 0]	[0, 2.440] [0, 0] [0, 0]
500	[0, 5] [0, 0] [0, 0]	[0, 5] [0, 0] [0, 0]	[0, 2.412] [0, 0] [0, 0]

Appendix A.2. Additional Figures

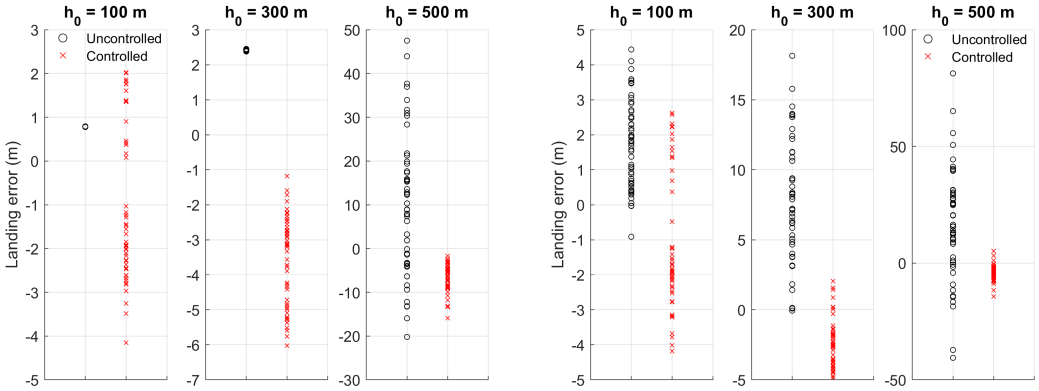

(**a**) Nominal wind speed at 6 m = 0 m/s

(**b**) Nominal wind speed at 6 m = 1 m/s

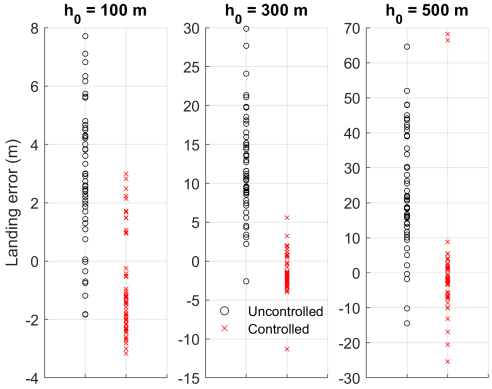

(**c**) Nominal wind speed at 6 m = 2 m/s

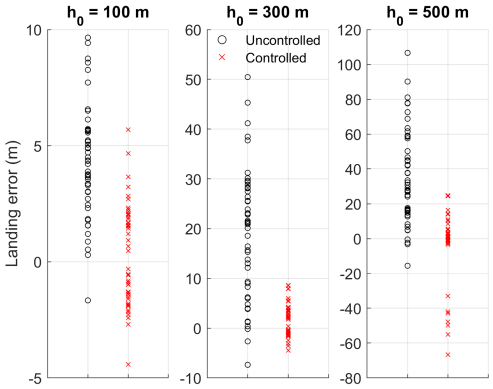

(**d**) Nominal wind speed at 6 m = 3 m/s

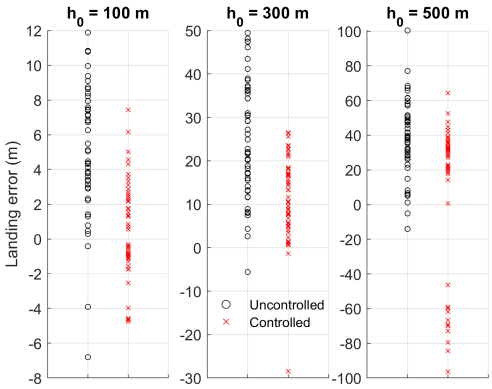

(**e**) Nominal wind speed at 6 m = 4 m/s

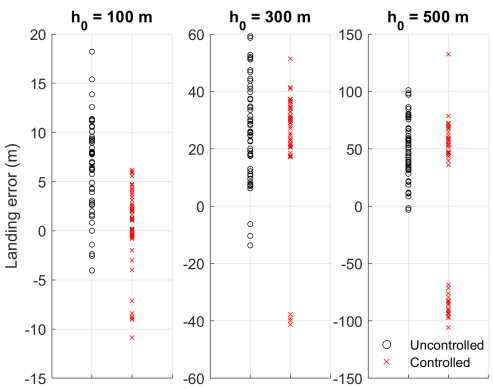

(**f**) Nominal wind speed at 6 m = 5 m/s

Figure A1. Landing position of system with no flare setting and standard LOS guidance, and uncontrolled system.

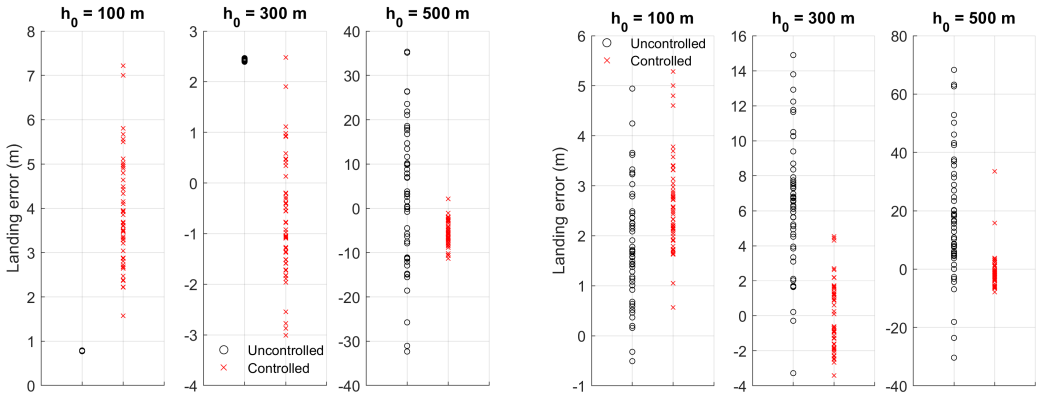

(**a**) Nominal wind speed at 6 m = 0 m/s (**b**) Nominal wind speed at 6 m = 1 m/s

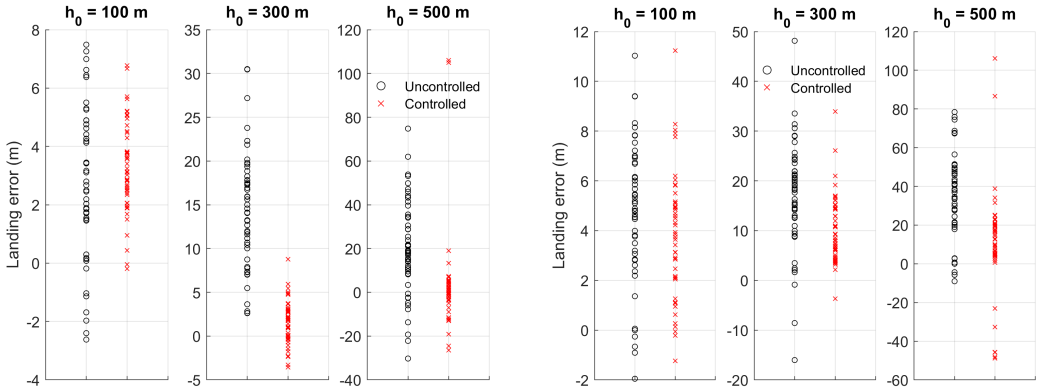

(**c**) Nominal wind speed at 6 m = 2 m/s (**d**) Nominal wind speed at 6 m = 3 m/s

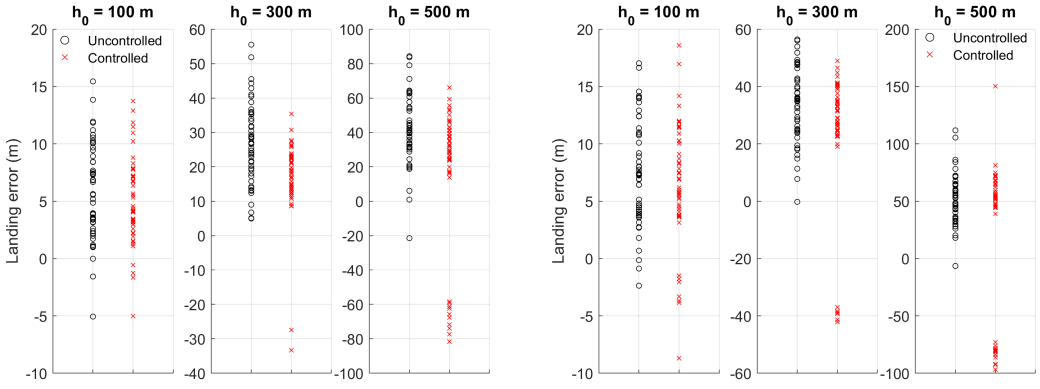

(**e**) Nominal wind speed at 6 m = 4 m/s (**f**) Nominal wind speed at 6 m = 5 m/s

Figure A2. Landing position of system with vertical velocity reduction flare setting and standard LOS guidance and uncontrolled system.

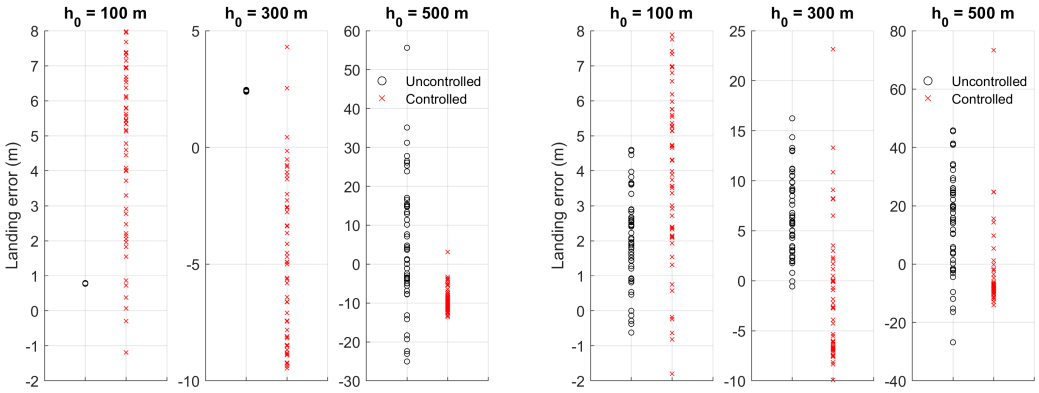

(**a**) Nominal wind speed at 6 m = 0 m/s (**b**) Nominal wind speed at 6 m = 1 m/s

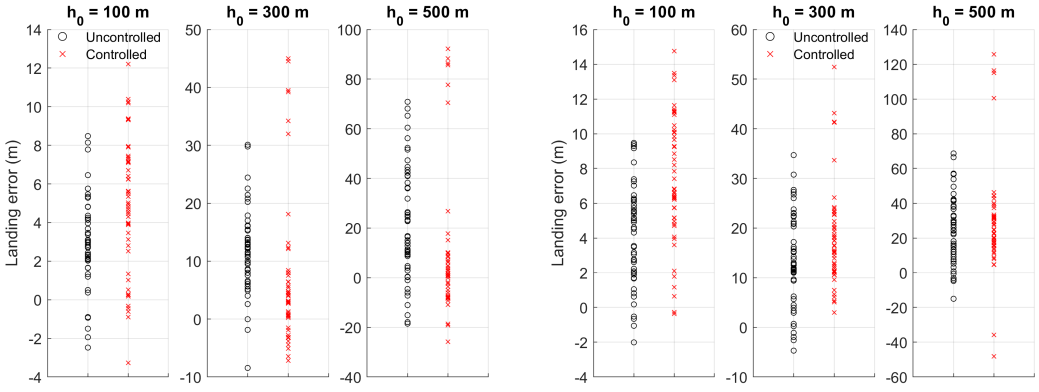

(**c**) Nominal wind speed at 6 m = 2 m/s (**d**) Nominal wind speed at 6 m = 3 m/s

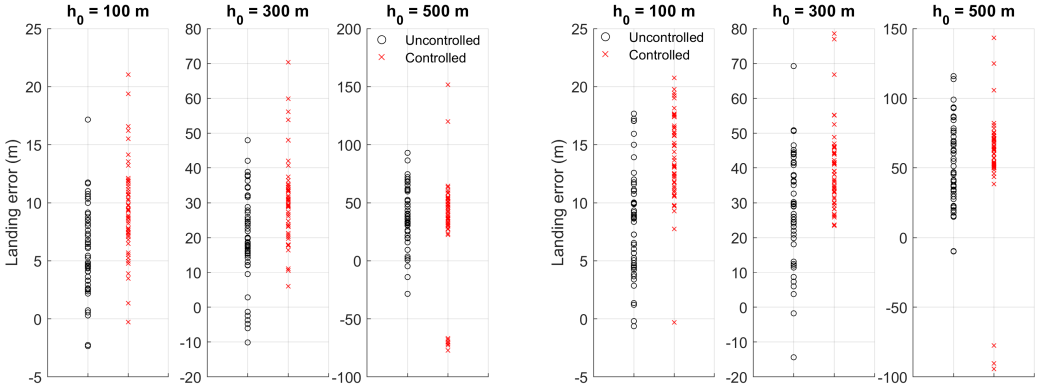

(**e**) Nominal wind speed at 6 m = 4 m/s (**f**) Nominal wind speed at 6 m = 5 m/s

Figure A3. Landing position of system with kinetic energy reduction flare setting and adaptive LOS guidance and uncontrolled system.

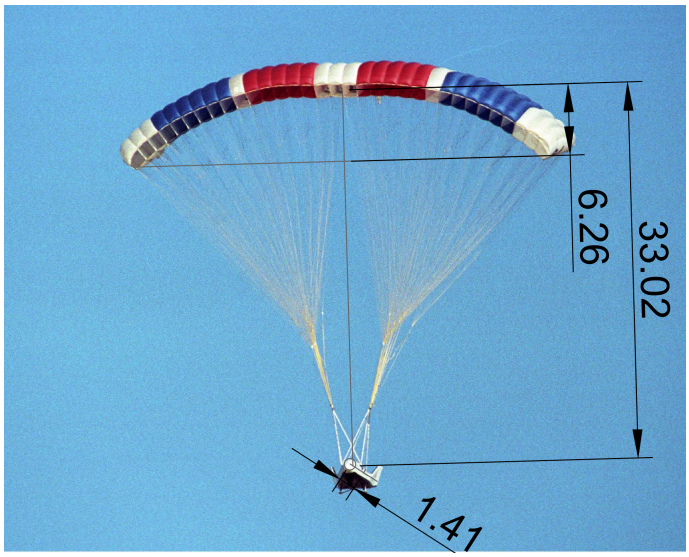

Figure A4. Determination of x, y, and z distances from the body axes centre to the parafoil axes centre in the NASA X-38 parafoil program. Note that the dimensions shown are scaled based on the 5500 ft^2 parafoil, but the image shows the 7700 ft^2 parafoil. Adapted from [23].

References

1. Federal Aviation Administration. *Advisory Circular: AC 21.17-4, Type Certification—Powered-Lift*; Technical Report; U.S. Department of Transportation: Washington, DC, USA, 2024.
2. Waimer, M.; Schatrow, P.; Lützenburger, M.; Wegener, N. Simulation studies on eVTOL crashworthiness in the conceptual and the preliminary design phase. In Proceedings of the Tenth Triennial International Aircraft Fire and Cabin Safety Research Conference, Atlantic City, NJ, USA, 17–20 October 2022.
3. Michalczyk, M.; Szcześniak, K. The model of vertical acceleration impact on backbone of member of the crew. *J. KONES* **2011**, *18*, 351–358.
4. Breivik, M.; Fossen, T.I. Principles of guidance-based path following in 2D and 3D. In Proceedings of the 44th IEEE Conference on Decision and Control, Seville, Spain, 12–15 December 2005; pp. 627–634. [CrossRef]
5. Li, Y.; Zhao, M.; Yao, M.; Chen, Q.; Guo, R.; Sun, T.; Jiang, T.; Zhao, Z. 6-DOF modeling and 3D trajectory tracking control of a powered parafoil system. *IEEE Access* **2020**, *8*, 151087–151105. [CrossRef]
6. Sun, H.; Sun, Q.; Tao, J.; Luo, S.; Chen, Z. A flight control system for parafoils based on improved PID control approach. In Proceedings of the 36th Chinese Control Conference (CCC), Dalian, China, 26–28 July 2017; pp. 1168–1173. [CrossRef]
7. Long, X.; Sun, M.; Piao, M.; Chen, Z. Parameterized trajectory optimization and tracking control of high altitude parafoil generation. *Energies* **2021**, *14*, 7460. [CrossRef]
8. Qu, S.T. Unmanned powered paraglider flight path control based on PID neutral network. *IOP Conf. Ser. Mater. Sci. Eng.* **2019**, *470*, 012008. [CrossRef]
9. Ward, M.; Gavrilovski, A.; Costello, M. Performance of an autonomous guided airdrop system with glide slope control. In Proceedings of the 21st AIAA Aerodynamic Decelerator Systems Technology Conference and Seminar, Dublin, Ireland, 23–26 May 2011; Number AIAA 2011-2572. [CrossRef]
10. Ward, M.; Costello, M. Adaptive glide slope control for parafoil and payload aircraft. *J. Guid. Control. Dyn.* **2013**, *36*, 1019–1034. [CrossRef]
11. Tao, J.; Dehmer, M.; Xie, G.; Zhou, Q. A generalized predictive control-based path following method for parafoil systems in wind environments. *IEEE Access* **2019**, *7*, 42586–42595. [CrossRef]
12. Tan, P.; Sun, Q.; Chen, Z.; Jiang, Y. Characteristic model–based generalized predictive control and its application to the parafoil and payload system. *Optim. Control Appl. Methods* **2019**, *40*, 659–675. [CrossRef]
13. Zhang, L.; Gao, H.; Chen, Z.; Sun, Q.; Zhang, X. Multi-objective global optimal parafoil homing trajectory optimization via Gauss pseudospectral method. *Nonlinear Dyn.* **2013**, *72*, 1–8. [CrossRef]
14. Leeman, A.; Preda, V.; Huertas, I.; Bennani, S. Autonomous parafoil precision landing using convex real-time optimized guidance and control. *CEAS Space J.* **2023**, *15*, 371–384. [CrossRef]
15. Yakimenko, O.; Slegers, N. Equations of Motion. In *Precision Aerial Delivery Systems: Modeling, Dynamics, and Control*; AIAA: Reston, VA, USA, 2015; Volume 248, Progress in Astronautics and Aeronautics, Chapter 5, pp. 263–352. [CrossRef]
16. Quadrelli, M.B.; Schutte, A.; Rimani, J.; Ermolli, L. Aero maneuvering dynamics and control for precision landing on Titan. In Proceedings of the 2019 IEEE Aerospace Conference, Big Sky, MT, USA, 2–9 March 2019. [CrossRef]

17. Lissaman, P.B.S.; Brown, G.J. Apparent mass effects on parafoil dynamics. In Proceedings of the Aerospace Design Conference, Irvine, CA, USA, 6–19 February 1993; Number AIAA 93-1236. [CrossRef]
18. Valdés, G. Urban Air Mobility Flight Dynamics. Master's Thesis, Cranfield University, Bedford, UK, 2020.
19. Wei, Z.; Gao, Y.; Shao, Z.; Wang, C. Dynamic-model-based closed-loop guidance and control for heavy parafoil system precision landing. *Aerosp. Sci. Technol.* **2024**, *146*, 108964. [CrossRef]
20. Madsen, C.; Sostaric, R.; Cerimele, C. Flight performance, aerodynamics, and simulation development for the X-38 parafoil test program. In Proceedings of the 17th AIAA Aerodynamic Decelerator Systems Technology Conference and Seminar, Monterey, CA, USA, 19–22 May 2003; Number AIAA 2003-2108. [CrossRef]
21. MathWorks. Wind Shear Model. 2024. Available online: https://uk.mathworks.com/help/aeroblks/windshearmodel.html (accessed on 2 August 2024).
22. *ADA123726*; MIL Standard and Handbook—Flying Qualities of Air Vehicles (MIL-F-8785C). Systems Technology Inc.: Hawthorne, CA, USA, 1992.
23. NASA. X-38 Image—EC01-0339-146. 2001. Available online: https://www.dfrc.nasa.gov/Gallery/Photo/X-38/Small/EC01-0339-146.jpg (accessed on 31 July 2024).

Disclaimer/Publisher's Note: The statements, opinions and data contained in all publications are solely those of the individual author(s) and contributor(s) and not of MDPI and/or the editor(s). MDPI and/or the editor(s) disclaim responsibility for any injury to people or property resulting from any ideas, methods, instructions or products referred to in the content.

https://dspace.org/

Autonomous parafoil flaring control system for eVTOL aircraft

Doran, Stephen; Souanef, Toufik; Whidborne, James F.

2025-02-01
MDPI
https://doi.org/10.3390/aerospace12020145
Doran S, Souanef T, Whidborne JF. (2025) Autonomous parafoil flaring control system for eVTOL aircraft. Aerospace, Volume 12, Issue 2, February 2025, Article number 145

Downloaded from a DSpace repository. https://dspace.org/